

This paper is a non-peer reviewed preprint submitted to EarthArXiv

Spatiotemporal forecast of extreme events in a chaotic dynamical model of slow slip events

Hojjat Kaveh,¹ Jean-Philippe Avouac,^{1,2} Andrew M Stuart³

¹Mechanical and Civil Engineering, California Institute of Technology, Pasadena.

²Geology and Planetary Science, California Institute of Technology, Pasadena.

³Computing and Mathematical Science, California Institute of Technology, Pasadena.

Key Points:

- Stress distribution on a fault self-organizes into a chaotic attractor, constraining the set of feasible prestresses before big events.
- Using model reduction, we find statistically feasible optimal prestress conditions that can lead to large events within a short time frame.
- Only with the current slip rate, we spatiotemporally forecast large events based on the proximity to the optimal prestress distributions.

Corresponding author: Hojjat Kaveh, hkaveh@caltech.edu

14 Abstract

15 Seismic and aseismic slip events result from episodic slips on faults and are often chaotic due to stress
 16 heterogeneity. Their predictability in nature is a widely open question. Here, we forecast extreme events in a
 17 numerical model of a single fault governed by rate-and-state friction, which produces realistic sequences of slow
 18 events with a wide range of magnitudes and inter-event times. The complex dynamics of this system arise from
 19 partial ruptures. As the system self-organizes, prestress is confined to a chaotic attractor of a relatively small
 20 dimension. We identify the instability regions (corresponding to particular stress distributions) within this at-
 21 tractor which are precursors of large events. We show that large events can be forecasted in time and space based
 22 on the determination of these instability regions in a low-dimensional space and the knowledge of the current
 23 slip rate on the fault.

24 Plain Language Summary

25 In a sequence of earthquakes or Slow Slip Events (SSEs), the stress on a fault goes through a complex
 26 evolution. This stress distribution often causes small partial ruptures, but sometimes triggers a full fault rup-
 27 ture. Identifying ‘dangerous’ stress conditions preceding a large rupture is crucial because a large rupture could
 28 occur if the fault’s stress aligns with these patterns. We propose a method to identify dangerous stress condi-
 29 tions on the fault that are also likely to be experienced by the fault’s evolution during the earthquake cycle. We
 30 parameterize dangerous stress conditions with a few scalars, both to ease the computational burden and to have
 31 an interpretable and useable predictive tool in the case of sparse data measurement that arises in real applica-
 32 tions. We test our method on a synthetic model of a Slow Slip sequence and show that using the closeness of
 33 the system to dangerous stress conditions, we can forecast large rupture events in time and space.

34 Introduction

35 Earthquakes and Slow Slip Events (SSEs) result from episodic frictional slip on the faults. Each slip event
 36 releases the elastic strain accumulated during an interevent period during which the fault is locked. This prin-
 37 ciple is often referred to as the elastic rebound theory in reference to (Reid, 1910). While the elastic rebound
 38 theory offers valuable insights into the long-term mean recurrence time of earthquakes and can be used for time-
 39 independent earthquake forecasting (Avouac, 2015; Marsan & Tan, 2020), it falls short of predicting the time
 40 or the magnitude of the larger events (Murray & Segall, 2002). The difficulty is that earthquakes often exhibit
 41 a chaotic behavior which is manifest in the irregular and rare occurrence of large slip events and various em-
 42 pirical scaling laws, such as the Gutenberg-Richter and the Omori laws (Scholz, 1989). The Gutenberg-Richter
 43 law (Gutenberg & Richter, 1950) states that earthquake magnitudes are distributed exponentially (the number
 44 of earthquakes with magnitude larger than M , $N(M)$, is given by $\log_{10} N(M) = a - bM$, where b is a scal-
 45 ing parameter of the order of one and a is a constant). The Omori law (Utsu et al., 1995) states that the rate of
 46 earthquakes during an aftershock sequence decays as $1/t$ where t is the time since the mainshock. Chaotic be-
 47 havior has also been identified in sequences of SSEs in Cascadia (Gualandi et al., 2020). These events obey the
 48 same scaling laws as regular earthquakes and produce very similar crack-like and pulse-like ruptures, although
 49 with several orders of magnitudes smaller slip rate and stress drop (Michel et al., 2019).

50 The main source of complexities in earthquake sequences is due to stress heterogeneities which can ei-
 51 ther be of static origin (due to faults geometry (Okubo & Aki, 1987), roughness (Sagy et al., 2007; Cattania,
 52 2019), or heterogeneity of mechanical properties (Kaneko et al., 2010)) or dynamic, due stress transfers among
 53 faults or within a single fault (Shaw & Rice, 2000). As the stress evolves during the earthquake cycle, it gen-
 54 erates asperities and barriers that can either facilitate a complete rupture of a fault (a system-size rupture) or im-
 55 pede the propagation of a rupture, resulting in a partial rupture. Partial or complete ruptures of a fault system

56 are therefore observed in nature (Konca et al., 2008). Large ruptures, though rare according to the Gutenberg-
57 Richter law, hold greater significance from a seismic hazard perspective.

58 Advances in the understanding of fault friction (Marone, 1998) and in numerical modeling of earthquake se-
59 quences (Rice, 1993; Lapusta et al., 2000; Lapusta & Liu, 2009) now make it possible to produce realistic sim-
60 ulations (Barbot et al., 2012). When performing those numerical simulations, initial conditions cannot be any
61 arbitrary value, and it is also crucial to recognize that certain initial conditions hold more statistical relevance
62 than others during the evolution of the dynamical system. For example, (Lapusta & Rice, 2003) and (Rubin &
63 Ampuero, 2005) advocate for conducting simulations over multiple seismic cycles to mitigate the influence of
64 arbitrary choices in initial conditions. In fact, the space of feasible stress distributions on a fault during earth-
65 quake cycles is significantly smaller than the space of arbitrary initial conditions, as the dynamical system self-
66 organizes into a chaotic attractor (Shaw & Rice, 2000). When a dynamical system converges to its chaotic at-
67 tractor, any state outside this attractor is not feasible within the system's evolution. Consequently, the space of
68 feasible states is limited to the attractor itself, resulting in a significantly smaller domain compared to the space
69 of any arbitrary states for the system.

70 Large events happen rarely in the chaotic evolution of the earthquake cycle so their forecast is extremely chal-
71 lenging. We hypothesize that as for other types of dynamical systems that produce extreme (or rare) events (Blonigan
72 et al., 2019; Farazmand & Sapsis, 2019), the trajectory of the dynamical system must traverse specific insta-
73 bility regions within the chaotic attractor for large fault ruptures to occur. These instability regions correspond
74 to the optimal distributions of stress (or the states of the frictional interface) that facilitate large ruptures and
75 are also accessible during the evolution of the system because they are part of the chaotic attractor. Despite con-
76 siderable research on deterministic chaos in earthquake cycle models (Huang & Turcotte, 1990; Becker, 2000;
77 Anghel et al., 2004; Kato, 2016; Barbot, 2019), certain essential features of the chaotic attractor, particularly
78 modes relevant to instability that are also statistically feasible, have remained elusive in the literature. This is
79 primarily due to the high-dimensional, chaotic, and multi-scale nature of the problem, as well as the rarity of
80 large events.

81 The identification of the optimal state of the frictional interface (prestress) that promotes large events, out of
82 all the statistically feasible distributions is the primary focus of this study. Following the approach of (Farazmand
83 & Sapsis, 2017), we use an approximation of the chaotic attractor of the system during the inter-event period;
84 this approximation uses Proper Orthogonal Decomposition (POD) to reduce dimension and account for the fea-
85 sibility constraint. Representing the optimal prestress in a low dimensional space is favorable for the purpose
86 of earthquake forecasting, as the data to constrain the physical parameters and current states of the system are
87 sparse for earthquake cycles. We use the proximity of the current slip rate of the system to the slip rates of op-
88 timal solutions to propose an effective forecast method of large events. Our results suggest that this framework
89 can be used to predict events in both space and time when we have access to the slip rate on the fault with cer-
90 tain resolution.

91 As our case study, we use a quasi-dynamic model with the standard rate-and-state friction with the aging law
92 (Ruina, 1983). We apply this methodology to a 2D fault within a 3D medium, using a model setup analog to
93 a model that has been shown to produce a realistic sequence of SSEs similar to those observed in Cascadia (Dal Zilio
94 et al., 2020). We limit the analysis to the case of SSEs as in that case a quasi-dynamic approximation is justi-
95 fied which speeds up the numerical simulations (Rice, 1993; Thomas et al., 2014). We benefit from the fact that
96 SSEs have a much larger ratio of nucleation size to the size of the fault compared to regular earthquakes. The
97 range of magnitude of events in our 1000 years of synthetic data is 5.6-7.4 whereas for a large fault system with
98 typical earthquakes, the range is much bigger. In other words, regular earthquake is a multi-scale process both
99 in time and space, whereas, SSEs in our simulation are only multi-scale in time. Spatially small-scale processes
100 in regular earthquakes contribute to more complexity of the system. This might limit the applicability of our
101 method to these events without any further considerations.

Results

Extreme events formulation

We use a quasi-dynamic model of slip events on a 2D finite fault in a 3D elastic medium, assuming rate-and-state friction with the aging law (reviewed in Supp A). The dynamical system describes the coupled evolution of two functions $V((x, y), t) : \Gamma \times \mathbb{R}^+ \rightarrow \mathbb{R}^+$ and $\theta((x, y), t) : \Gamma \times \mathbb{R}^+ \rightarrow \mathbb{R}^+$. $V((x, y), t)$ is the slip rate, and $\theta((x, y), t)$ is the state variable associated with the rate-and-state friction law, on the fault surface Γ at time $t \in \mathbb{R}^+$. We assume $u = [V, \theta]^\top$ belongs to an appropriately chosen function space $\mathcal{U} : (\Gamma \times \mathbb{R}^+) \times (\Gamma \times \mathbb{R}^+) \rightarrow \mathbb{R}^+ \times \mathbb{R}^+$ and characterizes the state of the frictional interface at any given time and position on the fault. In the context of rate-and-state friction, shear stress is a function of the combination of variables (V, θ) . Also, the evolution of the system is better rendered in the $\log_{10} u$ space. Consequently, we use the term ‘prestress’ to refer to the spatial distribution of $w = [\log_{10} V, \log_{10} \theta]^\top$ before a rupture; nonetheless, we formulate the dynamical model in terms of $u = (V, \theta)$.

The dynamical system for u is both multi-scale and chaotic and produces ruptures with a variety of sizes. The governing equation is

$$\frac{\partial u}{\partial t} = \mathcal{N}(u) \quad (1a)$$

$$u(x, y, 0) = u_0(x, y), \quad \forall (x, y) \in \Gamma \quad (1b)$$

where \mathcal{N} is a nonlinear differential operator¹ that encompasses the quasi-dynamic approximation of the elastodynamics and the friction law. We denote S^t as the solution operator for the dynamical system, mapping the current state forward by t time-units:

$$u(x, y, t) = S^t(u(x, y, 0)); \quad (2)$$

we can break this map into the components S_V^t and S_θ^t :

$$S^t(u(x, y, 0)) = [S_V^t(u(x, y, 0)), S_\theta^t(u(x, y, 0))]^\top \quad (3)$$

We assume that the dynamical system has a global attractor \mathcal{A} on which the dynamics are chaotic; we refer to this as the chaotic attractor in what follows.

Inspired by (Farazmand & Sapsis, 2019), we define event set $E(V_{\text{thresh}})$ for a prescribed threshold $V_{\text{thresh}} \in \mathbb{R}^+$ as:

$$E(V_{\text{thresh}}) = \{u \in \mathcal{U} : \sup_{(x, y) \in \Gamma} V(x, y) \geq V_{\text{thresh}}\} \quad (4)$$

By setting a proper event threshold (V_{thresh}), the event set includes both partial and full ruptures.

In practice, we consider a planar thrust fault with 90° dip angle in elastic half-space that consists of a Velocity-Weakening (VW) patch (dotted area in Fig 1 (a)), within which ruptures can nucleate and propagate, surrounded by a Velocity-Strengthening (VS) patch where the propagation of seismic ruptures is inhibited (Fig 1 (a)). The fault is loaded by a surrounding fault that slips at a constant rate.

For details on the physical model see Supp A. In short, we use a quasi-dynamic approximation of the elastodynamic problem of a rate-and-state frictional fault with the aging law formulation of the state variable evolution. The numerical simulations are run with the QDYN code which is an open-source boundary element software package to simulate earthquake sequences (Luo et al., 2017). The model, with properly selected and piecewise constant parameters and initial conditions, exhibits a complex sequence of events with a variety of magnitudes distributed with a heavy tail consistent with the Gutenberg-Richter law (Fig 1 (b)). The shear stress on the locked portion of the fault (Fig 1 (c)) increases during the interevent period, leading to elastic strain energy

¹ Technically a pseudo-differential operator

136 build-up. During episodic slip events, the shear stress drops, and elastic strain energy is released and dissipated
 137 by frictional sliding and the radiation damping (Fig 1 (c)). The time series of the sequence of partial rupture
 138 with rare large ruptures is plotted in Fig 1 (c,d). Since stress is a function of θ and V in the rate-and-state fric-
 139 tion, and θ is not measurable, we do not have access to stress distribution directly. As a result, in this work, we
 140 only assume that we have observations of the current slip rate when performing extreme event forecasting. In
 141 reality, the current slip rate on the fault can be indirectly constrained by measurements of ground surface dis-
 142 placements which involves an inversion that greatly reduces the spatial resolution of slip rate. Hence, we will
 143 also examine a simplified noisy scenario of slip rate measurement and study the performance of our algorithm
 144 with such condition. The slip potency deficit, which is the difference between the slip potency (integral of slip
 145 on the fault) and the slip potency if the fault was uniformly slipping at the loading rate, is plotted to show the
 146 chaotic behavior of the system and the rare occurrence of large events. The potency deficit builds up during the
 147 interevent period and drops during the episodic slip events (Fig 1 (e)). The time series of the magnitude of events
 148 is also plotted in Fig 1 (f).

149 We now seek to determine the optimal feasible distributions of $\log_{10} u$ (prestress) in the interevent pe-
 150 riod that for a prediction horizon T lead to large magnitude events. By a ‘feasible’ prestress, we mean a pre-
 151 stress that is inside the chaotic attractor of the system; a combination of V and θ that is likely to be realized dur-
 152 ing the evolution of the dynamical system. We also want our criteria for optimality of prestress to be low-dimensional
 153 so that it can be captured using observations that are typically sparse in reality. We then use our low-dimensional
 154 critical prestress and only the current measurable state of the system (slip rate, which can in principle be esti-
 155 mated from geodetic measurements) to forecast the time and location of a possible large event in a time win-
 156 dow horizon.

157 To formulate the question in mathematical terms, we introduce the moment magnitude of fault slip cumulated
 158 over the duration of integration Δt .

$$\widetilde{M}(u(x, y, t); \Delta t) = \frac{2}{3} \log_{10} \left(G \int_0^{\Delta t} \int_{\Gamma} S_V^{t'}(u(x, y, t)) dx dy dt' \right) - 6. \quad (5)$$

159 where G is the elastic shear modulus. \widetilde{M} measures the seismic moment on the fault in the \log_{10} scale during
 160 Δt time-units (Scholz, 1989). \widetilde{M} is slightly different from the definition of the moment magnitude (M) for one
 161 event because in \widetilde{M} , we take Δt to be a constant rather than being the actual duration of a particular event. In
 162 practice, we set it to be larger than the longest duration of events in our model. While we make use of \widetilde{M} in our
 163 problem setup and benefit from its continuity over u , we will report the performance of the forecast of extreme
 164 events with a regular definition of moment magnitude (M).

165 We next define a cost function:

$$F(u; \Delta t, T) = \sup_{t \in [0, T]} \widetilde{M}(S^t(u); \Delta t) \quad (6)$$

166 where function $F : \mathcal{U} \rightarrow \mathbb{R}$ takes u as input and, for a prescribed prediction horizon (T) and event duration
 167 (Δt), finds the largest moment magnitude generated by the initial condition u . The optimal (most dangerous)
 168 feasible prestress conditions are determined by finding the local maxima (U^*) of $F(u; \Delta t, T)$ over $u \in \mathcal{A} \setminus$
 169 $E(V_{\text{thresh}})$ through an optimization process:

$$U^* = \{u^* | u^* \in \mathcal{A} \setminus E(V_{\text{thresh}}), u^* \text{ is a local maximizer of } F(u; \Delta t, T), F(u^*; \Delta t, T) > F_e^*\} \quad (7)$$

170 where F_e^* is some threshold for the magnitude to define a ‘large’ event. Eq (7) encompasses the main question
 171 of this work; that is finding optimal and statistically feasible prestress on the fault during the interevent period
 172 that makes large events in a short time window. In Eq (7), $u^* \in \mathcal{A} \setminus E(V_{\text{thresh}})$ ensures that u^* is inside the
 173 chaotic attractor (statistical feasibility constraint) and also in the interevent period; any state (u^*) outside $\mathcal{A} \setminus$
 174 $E(V_{\text{thresh}})$ is inaccessible during the system’s evolution because of the self-organization. After solving the op-
 175 timization problem (Eq (7)), we use the ‘similarity’ of the current states of the system to solutions of Eq (7),

176 as an indicator of an upcoming large event. We use the current slip rate as our only knowledge of the current
 177 state of the system as θ is not measurable. Solutions to Eq (7) are instability regions inside the chaotic attrac-
 178 tor that generate large ruptures within the time span of $[0, T]$.
 179 Set $\mathcal{A} \setminus E(V_{\text{thresh}})$ is a complicated set in the high-dimensional function space \mathcal{U} . Even if we can solve this opti-
 180 mization problem in this large space, it would be impractical to represent prestress in this high-dimensional
 181 space because the sparse data generally available in reality can only yield a low-dimensional model of the slip
 182 rate distribution on a fault. As a result, we approximate this set with a simpler set, characterized in a low-dimensional
 183 space using the POD method. This approach is developed in the next part.

184 Model reduction and forecast scheme

185 Many high-dimensional chaotic dynamical systems can be approximated by a low-dimensional system
 186 (Taira et al., 2017; Rowley & Dawson, 2017; Li et al., 2023; Brandstätter et al., 1983). Although the underly-
 187 ing dynamics of earthquakes and Slow Slip cycles are often chaotic (Huang & Turcotte, 1990; Becker, 2000;
 188 Anghel et al., 2004; Kato, 2016; Barbot, 2019), in certain examples, it has been observed that the chaotic at-
 189 tractors are low dimensional (Gualandi et al., 2020, 2023) which mathematically implies that we can approx-
 190 imate the evolution of the sequence of events using parameters in a finite-dimensional space instead of an in-
 191 finite function space. We use this property to reduce the dimensionality and approximate the chaotic attractor
 192 during the interevent period.

193 We approximate and reduce the dimensionality of the chaotic attractor of the system during the inter-event pe-
 194 riod using the POD technique. The POD approach is widely adopted in the study of turbulent fluid flow (Taira
 195 et al., 2017); it is a linear model reduction method based on the singular value decomposition of the data co-
 196 variance matrix. The modes are ordered by the variance they capture in a dataset consisting of snapshot time
 197 series of the field. Since the evolution of the system is better realized in the $w = \log_{10} u$ space, we apply the
 198 POD on the w rather than u . We denote by \bar{w} the time average of the field (w) during the interevent period. POD
 199 technique inputs snapshots of $w - \bar{w}$ during the interevent period and gives orthonormal basis functions $\phi_i :$
 200 $\Gamma \times \Gamma \rightarrow \mathbb{R} \times \mathbb{R}$ and their associated variance λ_i for $i \geq 1$ where $\lambda_1 > \lambda_2 > \dots$ which quantifies the statisti-
 201 cal importance of each mode in the dataset. The subtraction of the mean is crucial because it ensures that the
 202 covariance matrix in the POD algorithm accurately reflects the variability and relationships within the dataset,
 203 rather than being influenced by the absolute positions of the data points. Then we can describe w , and conse-
 204 quently u , using a new coordinate system with the basis functions defined by ϕ_i 's. Since the basis functions are
 205 ordered by the variance they capture in the data, the truncation and approximation of the field $w - \bar{w}$, with the
 206 first N_m POD modes captures a maximal statistical relevance (in the variance sense) of data between all possi-
 207 ble N_m dimensional linear subspaces of $\log_{10} \mathcal{U}$.

208 We approximate $w : w \in \log_{10} (\mathcal{A} \setminus E(V_{\text{thresh}}))$ as perturbations around the time-average of w during the
 209 interevent period ($\bar{w} = [\bar{w}^V, \bar{w}^\theta]$) along those basis functions. Since we want to approximate only the interevent
 210 period we should exclude the event period ($E(V_{\text{thresh}})$) from the dataset of snapshots that are used to find POD
 211 modes (ϕ_i 's). Following (Blonigan et al., 2019), we constrain the perturbations along those eigenvectors to lie
 212 within a hyperellipse with a radius along each eigenvector proportional to the standard deviation of the data cap-
 213 tured by each mode. In other words, we allow more perturbation along those directions that capture more sta-
 214 tistical relevance in the data. The approximation of the chaotic attractor during the interevent period can be writ-
 215 ten as:

$$\log_{10} (\mathcal{A} \setminus E(V_{\text{thresh}})) \approx \left\{ \bar{w} + \sum_{i=1}^{N_m} a_i \phi_i \mid \sum_{i=1}^{N_m} \frac{a_i^2}{\lambda_i} \leq r_0^2 \right\}. \quad (8)$$

216 where ϕ_i 's ($i \geq 1$) are the orthonormal basis functions ordered by the data variance they capture (λ_i) in the
 217 centered dataset of time snapshots of $w - \bar{w}$ excluding the event period $E(V_{\text{thresh}})$. Here a_i is the amplitude
 218 of perturbation along ϕ_i and N_m is the number of basis functions we keep in our model reduction. The max-

imum perturbation along each basis function (ϕ_i) is constrained by the corresponding variance λ_i . One can play with the amplitude of the allowed perturbation which is represented by r_0 . Then Eq (7), which is an optimization problem in a high-dimensional function space \mathcal{U} , constrained on a complicated set $\mathcal{A} \setminus E(V_{\text{thresh}})$, can be approximated as an optimization problem in a low-dimensional (\mathbb{R}^{N_m}) space constrained within a hyperellipse. To solve the constrained optimization problem, we use optimal sampling in the framework of Bayesian optimization as it is useful when the objective function is costly to evaluate (Blanchard & Sapsis, 2021). The optimization method is described in Supp C. During the optimization process, we collect all optimal prestresses ($w^* = [(\log V)^*, (\log \theta)^*]^\top$) in a set W^* that satisfies the feasibility constraint ($w^* \in \log_{10}(\mathcal{A} \setminus E(V_{\text{thresh}}))$) and has the value of $F(10^{w^*}; \Delta t, T)$ above the threshold F_e^* :

$$W^* := \left\{ w^* = \bar{w} + \sum_{i=1}^{N_m} a_i \phi_i \mid \sum_{i=1}^{N_m} \frac{a_i^2}{\lambda_i} \leq r_0^2, F(10^{w^*}; \Delta t, T) > F_e^* \right\}. \quad (9)$$

W^* corresponds to the set of all of the prestresses leading to extreme events. To perform the spatial forecast, we need to record the evolution of each w^* for up to time T .

We use the proximity of the current state of the system to optimal states as an indicator of an upcoming large event. The current state of the system (w) is not measurable because θ is not measurable. Slip rate is the measurable component in w and we use it as a proxy of the current state of the system. Then, following (Blonigan et al., 2019), we use the maximum cosine similarity between the \log_{10} of the current slip rate ($\log V(t)$) and all of the optimal slip rates ($\log V_i^*$'s) in the set W^* as an indicator that signals an upcoming large event.

$$I(t) = \max_i \frac{\langle \log V(t) - \bar{w}^V, \log V_i^* - \bar{w}^V \rangle_{L^2}}{\| \log V(t) - \bar{w}^V \|_2 \| \log V_i^* - \bar{w}^V \|_2} \quad (10)$$

where $\langle \cdot, \cdot \rangle_{L^2}$ is the L^2 inner product, \bar{w}^V is the average slip rate during interevent periods in the dataset, $\log V_i^*$ is the velocity component of the i^{th} optimal prestress (w_i^*), and $\| \cdot \|_2$ is the L^2 norm. Note that $I(t)$ is only a function of the current slip rate on the fault. Here, we have assumed we have full access to the slip rate on the fault. We further study the case where we have a noisy slip rate measurement that is corrupted by a Gaussian low-pass filter. This is important because in reality the slip on the fault which comes from the inversion of surface displacement loses some spatial resolution due to smoothing in the inversion. We will demonstrate that the algorithm's performance degrades when there is a high level of noise in the slip rate.

In Supp D, we have studied a scenario in which the slip rate is known at only a few points on the fault. The results are almost as good as when we have full access to the slip rate on the fault because the slip evolution at neighboring points on the fault is strongly correlated due to elastic coupling. This result most likely benefits from large nucleation length for SSEs which is generally not true for earthquakes. The nucleation length for a 1D fault for mode III is given by $h_{ra} = \frac{2GD_{RS}b}{\pi\bar{\sigma}(b-a)^2}$ (Rubin & Ampuero, 2005), where G is shear modules, $\bar{\sigma}$ is the effective normal stress, and a, b, D_{RS} are frictional parameters and are presented in Supp A. For a 2D fault, the nucleation size is given by $h = (\pi^2/4)h_{ra}$ (Chen & Lapusta, 2009), and is $29.7(km)$ in our model, whereas the width of the VW zone is $W_{VW} = 25(km)$.

Extreme event forecast

We use a simulation run for a total duration of 2200 years. We exclude the initial 200 years to eliminate the transient behavior, letting the system converge to its chaotic attractor. To define the event set (Eq (4)), we set the event threshold $V_{\text{thresh}} = 5 \times 10^{-8}(m/s)$. The event threshold is chosen such that we get reasonable scaling properties and also, we don't lose many events. The time series of the maximum slip velocity on the fault is plotted in Supp A in which V_{thresh} is denoted by a dashed line. We use data from $t = 200$ to $t = 1200$ years to perform the model reduction and find basis functions ϕ_i 's and their corresponding variances λ_i 's. We approximate $\mathcal{A} \setminus E(V_{\text{thresh}})$ using Eq (8) with a number of modes $N_m = 13$ which capture more than 85% variance of the data (based on the discussion in Supp B). The mean of the field ($\bar{w} = [\bar{w}^V, \bar{w}^\theta]^\top$) together with the first four eigenfunctions $\phi_i = [\phi_i^V, \phi_i^\theta]^\top$ for interevent periods for the time range $t \in [200, 1200]$ (year)

260 are plotted in Fig (2) with \bar{w} as the empirical mean of the interevent states of the system w , ϕ_i^V as the i^{th} eigen-
 261 function of the $\log_{10} V$ and ϕ_i^θ as the i^{th} eigenfunction of the $\log_{10} \theta$. Using ϕ_i 's and λ_i 's, we solve the opti-
 262 mization problem which has T (prediction horizon), Δt (event duration), and r_0 (amount of perturbation around
 263 \bar{w}) as hyper-parameters. We set the prediction horizon to $T = 0.5(\text{year})$ and $\Delta t = 0.25(\text{year})$ as the max-
 264 imum duration of events in the time window of $t \in [200, 1200]$ year. With the increase of T , because of the
 265 effect of chaos, the predictability decreases and we would expect the performance of the algorithm to decrease.
 266 The value of r_0 in the Eq (8) controls the size of the hyperellipse which is the constraint of the optimization prob-
 267 lem. We performed the optimization for different values of r_0 . For perturbations constrained within a small hy-
 268 perellipse (small r_0), the algorithm does not find any optimal prestress that leads to a large event. This makes
 269 sense because, for small r_0 , w is close to the \bar{w} which is the average state of w during interevent periods. For
 270 very large r_0 , the approximation of $\mathcal{A} \setminus E(V_{\text{thresh}})$ with a hyperellipse is less valid because we let the pertur-
 271 bation have amplitudes much larger than the standard deviation of each component along each eigenfunction.
 272 So, one should find an intermediate r_0 whose values of the cost function at the local maxima are larger but close
 273 to the maximum magnitude observed in the dataset. Here, we report results for $r_0 = 3$ which means that we
 274 won't let the prestress go outside the total 3 standard deviation range from \bar{w} in \mathbb{R}^{N_m} . Unlike (Blonigan et al.,
 275 2019) that, for a fluid flow problem, found a unique solution for their similar optimization problem, we see con-
 276 vergence to multiple local maxima ($w^* = [(\log V)^*, (\log \theta)^*]^T$) for different algorithm initiations. As a re-
 277 sult, to make our algorithm robust, we solve the optimization problem multiple times with random initiations.
 278 The average prestress during the interevent period for the VW patch, and the prestress corresponding to one of
 279 the optimal solutions is plotted in Fig 3 (a,b). We have also plotted the dimensionless quantity $\log_{10}(V\theta/D_{RS})$
 280 in Fig 3 (c). The cumulative slip distribution corresponding to the event with magnitude 7.5 led by the opti-
 281 mal prestress is plotted in Fig 3 (d). We have plotted the slip rate (V), and the state variable (θ) corresponding
 282 to this particular optimal solution, together with the convergence of the optimization algorithm, in Supp C. We
 283 record the rupture extent of optimal solutions (a total of 12 local maxima) that have $F_e^* > 7.4$ to use for spa-
 284 tial prediction. These optimal prestress distributions are relatively complex with heterogeneities both along the
 285 strike and along the dip directions. Because we have only approximated the chaotic attractor by a hyperellipse,
 286 the solutions of the optimization problem are unlikely to be exactly observed in the simulation of the dynam-
 287 ical system evolution. However, because the non-linear dynamical system can be linearized locally, it can be
 288 assumed that if the system gets close to any of these optimal solutions, due to stress redistributions by events
 289 of all sizes, a slip event should follow with a head time (the difference between the current time and the time
 290 of occurrence of the large slip event) and a slip distribution close to this optimal solution. We rely on this prin-
 291 ciple to forecast the time and location of large slip events. It is interesting to note that with the defined event
 292 threshold, we don't see any full-system size rupture in the forward simulation. However, if we start from ho-
 293 mogeneous initial conditions, we see periodic fault-size ruptures. This solution is probably unstable or stable
 294 with a small basin of attraction because a relatively small perturbation from the homogeneous initial condition
 295 leads to the convergence of the system to its chaotic attractor.
 296 The indicator $I(t)$ (Eq (10)), can effectively forecast large events for the dataset from $t = 1200$ to $t = 2200$
 297 years with a prediction horizon of $T = 0.5$ (year). To illustrate, $I(t)$ is plotted alongside F in Fig 4 (a). A high
 298 value of F shows an upcoming large event in the time interval $[0, T]$ and we observe that when F rises, the in-
 299 dicator signals a large event by rising to large values. We define a threshold I_e above which we signal an up-
 300 coming large event. We also define F_e as the threshold for extreme events; whenever F is larger than F_e we say
 301 that an extreme event is going to happen in the next T year(s). The values of F_e and I_e are determined such that
 302 the proportion of the true positive and true negative forecasts of extreme events are maximized. By recording
 303 the values of $I(t)$ and $F(t)$, we can empirically find the conditional probability $P(F|I)$ (Fig 4 (b)). Values of
 304 F_e and I_e are denoted by the white vertical and horizontal dashed lines in Fig 4 (b). The probability in this con-
 305 text is with respect to the invariant measure of the chaotic attractor. Different quadrants of this plot show four
 306 conditions including true negative, false negative, true positive, and false positive from bottom left counterclock-
 307 wise to top left. While most of the high values of $P(F|I)$ lie inside the true negative and true positive regions,
 308 it is essential to acknowledge that the probabilities of false negative and false positive are not zero. We also plot

309 the empirical probability of observing an event greater than F_e given the knowledge of I , ($P[F > F_e|I]$). This
 310 value which is denoted by P_{ee} is plotted in Fig 4 (c). P_{ee} consistently rises to values close to one, which is an-
 311 other way to show that the indicator I can be used as a predictor of large events. We plot the forecast of rup-
 312 ture extent in Fig 4 (d) which shows the effectiveness of both spatial and temporal forecasts of large events. Since
 313 we have recorded the rupture extent of optimal solutions (elements in set W^*), as soon as the current state of
 314 the system gets close to the i^{th} optimal solution and the indicator signals an upcoming event ($I(t) > I_e$), we
 315 propose the recorded rupture extent of the i^{th} optimal solution as the spatial forecast. Fig 4 (e) shows the tem-
 316 poral forecast of events with the magnitude of events plotted in blue. Whenever the indicator has a value greater
 317 than I_e , we forecast (red region) that an event larger than $F_e = 6.9$ (black dashed line) will happen. Red shows
 318 the temporal prediction of events larger than F_e . The magnitude in Fig 4 (e) is calculated according to the reg-
 319 ular definition of the magnitude of an event (i.e. by integrating the slip velocity above the threshold over the
 320 exact duration of the event). In Supplemental Video 1, an animation of this prediction is available.

321 **Impact of Low-Pass Filter Noise on Prediction Accuracy**

322 In this part, we illustrate a limitation of our method as we lose more and more information with noisier
 323 data. Real-world slip inversion on the fault has inherent low-pass filter noise because the process of finding slip
 324 on the fault from surface displacements involves filtering techniques that inevitably introduce this type of noise.
 325 These techniques are necessary due to the measurement limitations, which cannot capture high-frequency vari-
 326 ations accurately, leading to a smoother and potentially less precise representation of the actual slip rates. We
 327 apply a Gaussian kernel to the synthetic slip rate data, mimicking the characteristics of realistic datasets. This
 328 approach allows us to systematically assess the impact of noise on the performance of extreme event predic-
 329 tion. By varying the standard deviation of the Gaussian kernel, we evaluate how different noise levels affect the
 330 algorithm's accuracy. The standard deviation is expressed in a dimensionless form relative to the width of the
 331 width of the VW zone.

332 We assume that the slip rate is corrupted by a Gaussian kernel which is defined mathematically as:

$$G(x, y) = \frac{1}{2\pi\sigma^2} \exp\left(-\frac{x^2 + y^2}{2\sigma^2}\right). \quad (11)$$

333 where σ is the standard deviation of the Gaussian kernel, controlling the extent of the smoothing effect. By con-
 334 volving this kernel with the original slip rate data $V(x, y)$, we obtain the noisy slip rate $V'(x, y)$:

$$V'(x, y) = \int_{\Gamma} V(x', y') \cdot G(x - x', y - y') dx' dy' \quad (12)$$

335 To visually demonstrate the effect of the kernel on the data, we plotted one snapshot of slip rate without noise
 336 in Fig 5 (a) and then applied the low-pass filter with different standard deviation on that snapshot of the veloc-
 337 ity and plot them in Fig 5 (b,c,d). The conditional probability $P(F|I)$ for a 1000 year long data that are cor-
 338 rupted by these noise levels are plotted in Fig 5 (e,f,g). As the noise level increases the probability mass in the
 339 upper left (false positive) and lower right (false negative) increases. Fig 5 (f) and (g) show that with a standard
 340 deviation greater than $0.5W_{VW}$, we have a large probability of a false signal. This is a limitation of our work
 341 and potentially considering more POD modes, using data assimilation techniques to more accurately invert for
 342 slip on the fault, and considering the history of the time series are some of the methods that can be used to im-
 343 prove the performance when the noise level is large.

344 **Discussion**

345 This study demonstrates the possibility of predicting the time, size, and spatial extent of extreme events
 346 in a simplified dynamical model of earthquake sequences based on the instantaneous observation of fault slip
 347 rate. The proposed approach was adapted from a technique developed to forecast extreme events in turbulent

348 fluid flow (Farazmand & Sapsis, 2017; Blonigan et al., 2019). By constraining the prestress on a fault to the only
 349 feasible ones and solving an optimization problem, we found the optimal prestress in a low dimensional space.
 350 Optimal prestress refers to configurations of stress heterogeneity on the fault triggering large events within small
 351 time windows. Identifying the optimal prestress distributions that are also statistically accessible during the earth-
 352 quake cycle is pivotal.

353 Prestress self-organizes into a chaotic attractor which occupies only a small fraction of all possible stress
 354 distributions on the fault. The identification of the optimal prestress within this reduced set is crucial for two
 355 reasons. First, it helps establish a low-dimensional representation of optimal prestress; the significance of reduced-
 356 order proxy of critical prestress is even more important for earthquakes than SSEs, primarily due to the scarcity
 357 of observational data obtained from paleoseismic records. Second, everything outside this set remains unseen
 358 during the earthquake cycle's evolution. If that was not the case, the space of hypothetical stress distribution
 359 possibly leading to large events would be intractable.

360 Our finding suggests that the chaotic nature of earthquake sequences is not an insurmountable obstacle
 361 to time-dependent earthquake forecasting. However, we acknowledge that we considered a favorable model setup
 362 designed to produce SSEs. It would be now interesting to test this approach in the case of a model setup pro-
 363 ducing regular earthquakes (i.e., with slip rates of 1cm/s to 1m/s to be comparable to real earthquakes) with
 364 larger ratios of fault dimensions to nucleation size and with a larger range of earthquake magnitudes (Barbot, 2021; Cattani
 365 This is doable although computationally challenging. The amplitude of the stress heterogeneity would be more
 366 substantial for regular earthquakes, where dynamic wave-mediated stresses allow for rupture propagation over
 367 lower stress conditions than for aseismic slip, particularly in models with stronger dynamic weakening or with
 368 persistent heterogeneity such as normal stress perturbations. (Noda et al., 2009; Lambert et al., 2021) .

369 It is expected that earthquake sequences would then show more complexity due to the cascading effects
 370 which are responsible for foreshocks and aftershocks in natural earthquake sequences, and which are not present
 371 in our simulations. In that regard, (Blonigan et al., 2019) reported that the performance of their prediction of
 372 rare events diminishes with the increase in Reynolds number in their turbulent flow case. It is possible that we
 373 have the same limitation as the ratio of the nucleation size to the dimensions of the fault decreases.

374 Additionally, slip rate data of a fault is determined through the inversion of surface displacement, which
 375 results in low spatial resolution. In our synthetic test, we studied the performance of extreme event prediction
 376 when the synthetic slip rate is corrupted by a low pass filter. Our results indicated that predictability is compro-
 377 mised when the standard deviation of the low-pass filter kernel gets larger and larger. This finding highlights
 378 a limitation in the application of our study in its current form when this type of noise is prevalent in the data.
 379 Addressing this limitation will be a focus of our future work. Potential approaches include incorporating ad-
 380 ditional components into the extreme event criteria and solving a data assimilation problem, such as using the
 381 Ensemble Kalman filter, to more accurately invert for slip rates on the fault.

382 Data Availability Statement

383 We used a model of a 2D thrust fault in a 3D medium governed by rate-and-state friction with aging law
 384 for the evolution of state variable (θ). The forward model is briefly reviewed in Supp A. The model parame-
 385 ters are summarized in Table A1. To simulate the forward model, we use the [QDYN software](https://github.com/ydluo/qdyn)², which is an open-
 386 source code to simulate earthquake cycles (Luo et al., 2017). We use the POD technique to reduce the dimen-
 387 sionality of the problem. This method is reviewed in Supp B. To solve the optimization problem we use the Bayesian

² <https://github.com/ydluo/qdyn>

388 optimization method (Brochu et al., 2010; Blanchard & Sapsis, 2021) that is reviewed in Supp C. We used the
389 open source code available on [GitHub](#)³ for solving the optimization problem.

390 **Supplementary Materials**

391 Supp A Model

392 Supp B Proper Orthogonal Decomposition (POD): method and result

393 Supp C Optimization

394 Supp D Forecast with Partial Observation of Slip Rate

395 Supplemental Figures: Fig Supp1 to Supp5

396 Supplemental Videos: Movie S1 to Movie S2

³ <https://github.com/ablancha/gpsearch>

397

References

- 398 Anghel, M., Ben-Zion, Y., & Rico-Martinez, R. (2004). Dynamical System Analysis and Forecasting of
399 Deformation Produced by an Earthquake Fault. In A. Donnellan, P. Mora, M. Matsu'ura, & X.-c. Yin
400 (Eds.), *Computational Earthquake Science Part I* (pp. 2023–2051). Basel: Birkhäuser. Retrieved 2023-
401 2023-06-29, from https://doi.org/10.1007/978-3-0348-7873-9_15 doi: 10.1007/
402 978-3-0348-7873-9_15
- 403 Avouac, J.-P. (2015). From Geodetic Imaging of Seismic and Aseismic Fault Slip to Dynamic Modeling of
404 the Seismic Cycle. *Annual Review of Earth and Planetary Sciences*, *43*(1), 233–271. Retrieved 2023-
405 07-23, from <https://doi.org/10.1146/annurev-earth-060614-105302> (eprint:
406 <https://doi.org/10.1146/annurev-earth-060614-105302>) doi: 10.1146/annurev-earth-060614-105302
- 407 Barbot, S. (2019, October). Slow-slip, slow earthquakes, period-two cycles, full and partial ruptures,
408 and deterministic chaos in a single asperity fault. *Tectonophysics*, *768*, 228171. Retrieved
409 2022-12-06, from [https://www.sciencedirect.com/science/article/pii/
410 S0040195119302781](https://www.sciencedirect.com/science/article/pii/S0040195119302781) doi: 10.1016/j.tecto.2019.228171
- 411 Barbot, S. (2021, April). A Spectral Boundary-Integral Method for Quasi-Dynamic Ruptures of Multi-
412 Parallel Faults. *Bulletin of the Seismological Society of America*, *111*(3), 1614–1630. Retrieved
413 2024-06-13, from <https://doi.org/10.1785/0120210004> doi: 10.1785/0120210004
- 414 Barbot, S., Lapusta, N., & Avouac, J.-P. (2012, May). Under the Hood of the Earthquake Machine: Toward
415 Predictive Modeling of the Seismic Cycle. *Science*, *336*(6082), 707–710. Retrieved 2023-07-23,
416 from <https://www.science.org/doi/10.1126/science.1218796> (Publisher: Amer-
417 ican Association for the Advancement of Science) doi: 10.1126/science.1218796
- 418 Becker, T. W. (2000). Deterministic Chaos in two State-Variable Friction Sliders and the Ef-
419 fect of Elastic Interactions. In *Geocomplexity and the Physics of Earthquakes* (pp. 5–
420 26). American Geophysical Union (AGU). Retrieved 2023-06-29, from [https://
421 onlinelibrary.wiley.com/doi/abs/10.1029/GM120p0005](https://onlinelibrary.wiley.com/doi/abs/10.1029/GM120p0005) (eprint:
422 <https://onlinelibrary.wiley.com/doi/pdf/10.1029/GM120p0005>) doi: 10.1029/GM120p0005
- 423 Blanchard, A., & Sapsis, T. (2021, January). Bayesian optimization with output-weighted optimal sam-
424 pling. *Journal of Computational Physics*, *425*, 109901. Retrieved 2023-02-16, from [https://www
425 .sciencedirect.com/science/article/pii/S0021999120306756](https://www.sciencedirect.com/science/article/pii/S0021999120306756) doi: 10.1016/j.
426 jcp.2020.109901
- 427 Blonigan, P. J., Farazmand, M., & Sapsis, T. P. (2019, April). Are extreme dissipation events predictable
428 in turbulent fluid flows? *Physical Review Fluids*, *4*(4), 044606. Retrieved 2022-12-09, from
429 <https://link.aps.org/doi/10.1103/PhysRevFluids.4.044606> (Publisher:
430 American Physical Society) doi: 10.1103/PhysRevFluids.4.044606
- 431 Brandstätter, A., Swift, J., Swinney, H. L., Wolf, A., Farmer, J. D., Jen, E., & Crutchfield, P. J. (1983, Octo-
432 ber). Low-Dimensional Chaos in a Hydrodynamic System. *Physical Review Letters*, *51*(16), 1442–
433 1445. Retrieved 2023-06-29, from [https://link.aps.org/doi/10.1103/PhysRevLett
434 .51.1442](https://link.aps.org/doi/10.1103/PhysRevLett.51.1442) (Publisher: American Physical Society) doi: 10.1103/PhysRevLett.51.1442
- 435 Brochu, E., Cora, V. M., & de Freitas, N. (2010, December). *A Tutorial on Bayesian Optimization of
436 Expensive Cost Functions, with Application to Active User Modeling and Hierarchical Reinforce-
437 ment Learning*. arXiv. Retrieved 2024-02-04, from <http://arxiv.org/abs/1012.2599>
438 (arXiv:1012.2599 [cs]) doi: 10.48550/arXiv.1012.2599
- 439 Cattania, C. (2019). Complex Earthquake Sequences On Simple Faults. *Geophysical Re-
440 search Letters*, *46*(17-18), 10384–10393. Retrieved 2023-06-28, from [https://
441 onlinelibrary.wiley.com/doi/abs/10.1029/2019GL083628](https://onlinelibrary.wiley.com/doi/abs/10.1029/2019GL083628) (eprint:
442 <https://onlinelibrary.wiley.com/doi/pdf/10.1029/2019GL083628>) doi: 10.1029/2019GL083628
- 443 Chen, T., & Lapusta, N. (2009). Scaling of small repeating earthquakes explained by interaction of seis-
444 mic and aseismic slip in a rate and state fault model. *Journal of Geophysical Research: Solid Earth*,
445 *114*(B1). Retrieved 2023-05-24, from <https://onlinelibrary.wiley.com/doi/abs/10>

- 446 .1029/2008JB005749 (eprint: <https://onlinelibrary.wiley.com/doi/pdf/10.1029/2008JB005749>)
 447 doi: 10.1029/2008JB005749
- 448 Dal Zilio, L., Lapusta, N., & Avouac, J. (2020, May). Unraveling Scaling Properties of Slow-Slip Events.
 449 *Geophysical Research Letters*, 47(10). Retrieved 2023-01-17, from [https://onlinelibrary](https://onlinelibrary.wiley.com/doi/10.1029/2020GL087477)
 450 [.wiley.com/doi/10.1029/2020GL087477](https://onlinelibrary.wiley.com/doi/10.1029/2020GL087477) doi: 10.1029/2020GL087477
- 451 Farazmand, M., & Sapsis, T. P. (2017, September). A variational approach to probing extreme events
 452 in turbulent dynamical systems. *Science Advances*, 3(9), e1701533. Retrieved 2022-12-09, from
 453 <https://www.science.org/doi/full/10.1126/sciadv.1701533> (Publisher:
 454 American Association for the Advancement of Science) doi: 10.1126/sciadv.1701533
- 455 Farazmand, M., & Sapsis, T. P. (2019, August). Extreme Events: Mechanisms and Prediction. *Ap-*
 456 *plied Mechanics Reviews*, 71(5). Retrieved 2022-12-09, from [https://doi.org/10.1115/1](https://doi.org/10.1115/1.4042065)
 457 [.4042065](https://doi.org/10.1115/1.4042065) doi: 10.1115/1.4042065
- 458 Geubelle, P. H., & Rice, J. R. (1995, November). A spectral method for three-dimensional elastody-
 459 namic fracture problems. *Journal of the Mechanics and Physics of Solids*, 43(11), 1791–1824.
 460 Retrieved 2022-12-07, from [https://www.sciencedirect.com/science/article/](https://www.sciencedirect.com/science/article/pii/002250969500043I)
 461 [pii/002250969500043I](https://www.sciencedirect.com/science/article/pii/002250969500043I) doi: 10.1016/0022-5096(95)00043-I
- 462 Gualandi, A., Avouac, J.-P., Michel, S., & Faranda, D. (2020, July). The predictable chaos of slow
 463 earthquakes. *Science Advances*, 6(27), eaaz5548. Retrieved 2022-12-10, from [https://](https://www.science.org/doi/10.1126/sciadv.aaz5548)
 464 www.science.org/doi/10.1126/sciadv.aaz5548 (Publisher: American Associa-
 465 tion for the Advancement of Science) doi: 10.1126/sciadv.aaz5548
- 466 Gualandi, A., Faranda, D., Marone, C., Cocco, M., & Mengaldo, G. (2023, February). Deterministic and
 467 stochastic chaos characterize laboratory earthquakes. *Earth and Planetary Science Letters*, 604,
 468 117995. Retrieved 2023-06-28, from [https://www.sciencedirect.com/science/](https://www.sciencedirect.com/science/article/pii/S0012821X23000080)
 469 [article/pii/S0012821X23000080](https://www.sciencedirect.com/science/article/pii/S0012821X23000080) doi: 10.1016/j.epsl.2023.117995
- 470 Gutenberg, B., & Richter, C. F. (1950, April). Seismicity of the Earth and associated phenom-
 471 ena. *MAUSAM*, 1(2), 174–176. Retrieved 2023-12-26, from [https://mausamjournal](https://mausamjournal.imd.gov.in/index.php/MAUSAM/article/view/4568)
 472 [.imd.gov.in/index.php/MAUSAM/article/view/4568](https://mausamjournal.imd.gov.in/index.php/MAUSAM/article/view/4568) (Number: 2) doi:
 473 10.54302/mausam.v1i2.4568
- 474 Huang, J., & Turcotte, D. L. (1990). Are earthquakes an example of deterministic chaos? *Geo-*
 475 *physical Research Letters*, 17(3), 223–226. Retrieved 2023-06-29, from [https://](https://onlinelibrary.wiley.com/doi/abs/10.1029/GL017i003p00223)
 476 onlinelibrary.wiley.com/doi/abs/10.1029/GL017i003p00223 (eprint:
 477 <https://onlinelibrary.wiley.com/doi/pdf/10.1029/GL017i003p00223>) doi: 10.1029/
 478 GL017i003p00223
- 479 Kaneko, Y., Avouac, J.-P., & Lapusta, N. (2010, May). Towards inferring earthquake patterns from geode-
 480 tic observations of interseismic coupling. *Nature Geoscience*, 3(5), 363–369. Retrieved 2023-07-23,
 481 from <https://www.nature.com/articles/ngeo843> (Number: 5 Publisher: Nature Pub-
 482 lishing Group) doi: 10.1038/ngeo843
- 483 Kato, N. (2016, June). Earthquake Cycles in a Model of Interacting Fault Patches: Complex Behavior at
 484 Transition from Seismic to Aseismic Slip. *Bulletin of the Seismological Society of America*, 106(4),
 485 1772–1787. Retrieved 2023-06-29, from <https://doi.org/10.1785/0120150185> doi: 10
 486 .1785/0120150185
- 487 Konca, A. O., Avouac, J.-P., Sladen, A., Meltzner, A. J., Sieh, K., Fang, P., ... Helmberger, D. V.
 488 (2008, December). Partial rupture of a locked patch of the Sumatra megathrust during the 2007
 489 earthquake sequence. *Nature*, 456(7222), 631–635. Retrieved 2023-07-23, from [https://](https://www.nature.com/articles/nature07572)
 490 www.nature.com/articles/nature07572 (Number: 7222 Publisher: Nature Publishing
 491 Group) doi: 10.1038/nature07572
- 492 Lambert, V., & Lapusta, N. (2021). Resolving Simulated Sequences of Earthquakes and Fault
 493 Interactions: Implications for Physics-Based Seismic Hazard Assessment. *Journal of Geo-*
 494 *physical Research: Solid Earth*, 126(10), e2021JB022193. Retrieved 2024-06-13, from

- 495 <https://onlinelibrary.wiley.com/doi/abs/10.1029/2021JB022193> (eprint:
496 <https://onlinelibrary.wiley.com/doi/pdf/10.1029/2021JB022193>) doi: 10.1029/2021JB022193
- 497 Lambert, V., Lapusta, N., & Faulkner, D. (2021). Scale Dependence of Earthquake Rupture Pre-
498 stress in Models With Enhanced Weakening: Implications for Event Statistics and Inferences
499 of Fault Stress. *Journal of Geophysical Research: Solid Earth*, 126(10), e2021JB021886. Re-
500 trieved 2024-06-13, from [https://onlinelibrary.wiley.com/doi/abs/10.1029/
501 2021JB021886](https://onlinelibrary.wiley.com/doi/abs/10.1029/2021JB021886) (eprint: <https://onlinelibrary.wiley.com/doi/pdf/10.1029/2021JB021886>) doi:
502 10.1029/2021JB021886
- 503 Lapusta, N., & Liu, Y. (2009). Three-dimensional boundary integral modeling of spontaneous earth-
504 quake sequences and aseismic slip. *Journal of Geophysical Research: Solid Earth*, 114(B9). Re-
505 trieved 2023-01-12, from [https://onlinelibrary.wiley.com/doi/abs/10.1029/
506 2008JB005934](https://onlinelibrary.wiley.com/doi/abs/10.1029/2008JB005934) (eprint: <https://onlinelibrary.wiley.com/doi/pdf/10.1029/2008JB005934>) doi:
507 10.1029/2008JB005934
- 508 Lapusta, N., & Rice, J. R. (2003). Nucleation and early seismic propagation of small and large events
509 in a crustal earthquake model. *Journal of Geophysical Research: Solid Earth*, 108(B4). Re-
510 trieved 2023-06-28, from [https://onlinelibrary.wiley.com/doi/abs/10.1029/
511 2001JB000793](https://onlinelibrary.wiley.com/doi/abs/10.1029/2001JB000793) (eprint: <https://onlinelibrary.wiley.com/doi/pdf/10.1029/2001JB000793>) doi:
512 10.1029/2001JB000793
- 513 Lapusta, N., Rice, J. R., Ben-Zion, Y., & Zheng, G. (2000). Elastodynamic analysis for slow tectonic
514 loading with spontaneous rupture episodes on faults with rate- and state-dependent friction. *Jour-
515 nal of Geophysical Research: Solid Earth*, 105(B10), 23765–23789. Retrieved 2023-07-23, from
516 <https://onlinelibrary.wiley.com/doi/abs/10.1029/2000JB900250> (eprint:
517 <https://onlinelibrary.wiley.com/doi/pdf/10.1029/2000JB900250>) doi: 10.1029/2000JB900250
- 518 Li, M., Jain, S., & Haller, G. (2023, May). Model reduction for constrained mechanical systems via
519 spectral submanifolds. *Nonlinear Dynamics*, 111(10), 8881–8911. Retrieved 2023-06-29, from
520 <https://doi.org/10.1007/s11071-023-08300-5> doi: 10.1007/s11071-023-08300-5
- 521 Luo, Y., Ampuero, J. P., Galvez, P., Ende, M. v. d., & Idini, B. (2017, February). *QDYN: a Quasi-DYNAMIC*
522 *earthquake simulator (v1.1)*. Zenodo. Retrieved 2023-07-15, from [https://zenodo.org/
523 record/322459](https://zenodo.org/record/322459) doi: 10.5281/zenodo.322459
- 524 Marone, C. (1998). Laboratory-Derived Friction Laws and Their Application to Seismic Fault-
525 ing. *Annual Review of Earth and Planetary Sciences*, 26(1), 643–696. Retrieved 2023-
526 12-27, from <https://doi.org/10.1146/annurev.earth.26.1.643> (eprint:
527 <https://doi.org/10.1146/annurev.earth.26.1.643>) doi: 10.1146/annurev.earth.26.1.643
- 528 Marsan, D., & Tan, Y. J. (2020, March). Maximum Earthquake Size and Seismicity Rate from an
529 ETAS Model with Slip Budget. *Bulletin of the Seismological Society of America*, 110(2), 874–
530 885. Retrieved 2023-12-26, from <https://doi.org/10.1785/0120190196> doi:
531 10.1785/0120190196
- 532 Michel, S., Gualandi, A., & Avouac, J.-P. (2019, October). Similar scaling laws for earthquakes and Cas-
533 cadia slow-slip events. *Nature*, 574(7779), 522–526. Retrieved 2023-07-10, from [https://www
534 .nature.com/articles/s41586-019-1673-6](https://www.nature.com/articles/s41586-019-1673-6) (Number: 7779 Publisher: Nature Publish-
535 ing Group) doi: 10.1038/s41586-019-1673-6
- 536 Murray, J., & Segall, P. (2002, September). Testing time-predictable earthquake recurrence by direct mea-
537 surement of strain accumulation and release. *Nature*, 419(6904), 287–291. Retrieved 2023-12-
538 26, from <https://www.nature.com/articles/nature00984> (Number: 6904 Publisher:
539 Nature Publishing Group) doi: 10.1038/nature00984
- 540 Noda, H., Dunham, E. M., & Rice, J. R. (2009). Earthquake ruptures with thermal weakening and the
541 operation of major faults at low overall stress levels. *Journal of Geophysical Research: Solid Earth*,
542 114(B7). Retrieved 2023-07-15, from [https://onlinelibrary.wiley.com/doi/abs/10
543 .1029/2008JB006143](https://onlinelibrary.wiley.com/doi/abs/10.1029/2008JB006143) (eprint: <https://onlinelibrary.wiley.com/doi/pdf/10.1029/2008JB006143>)

- doi: 10.1029/2008JB006143
- 544 Okubo, P. G., & Aki, K. (1987). Fractal geometry in the San Andreas Fault System. *Journal of Geophysical Research: Solid Earth*, 92(B1), 345–355. Retrieved 2023-06-28, from
 545 <https://onlinelibrary.wiley.com/doi/abs/10.1029/JB092iB01p00345>
 546 (_eprint: <https://onlinelibrary.wiley.com/doi/pdf/10.1029/JB092iB01p00345>) doi: 10.1029/
 547 JB092iB01p00345
- 548 Reid, H. (1910). *The Mechanics of the Earthquake, The California Earthquake of April 18, 1906, Report of*
 549 *the State Investigation Commission* (Vol. 2).
- 550 Rice, J. R. (1993). Spatio-temporal complexity of slip on a fault. *Journal of Geophysical*
 551 *Research: Solid Earth*, 98(B6), 9885–9907. Retrieved 2023-04-20, from [https://](https://onlinelibrary.wiley.com/doi/abs/10.1029/93JB00191)
 552 onlinelibrary.wiley.com/doi/abs/10.1029/93JB00191 (_eprint:
 553 <https://onlinelibrary.wiley.com/doi/pdf/10.1029/93JB00191>) doi: 10.1029/93JB00191
- 554 Rowley, C. W., & Dawson, S. T. (2017). Model Reduction for Flow Analysis and Control. *Annual*
 555 *Review of Fluid Mechanics*, 49(1), 387–417. Retrieved 2023-06-29, from [https://doi.org/](https://doi.org/10.1146/annurev-fluid-010816-060042)
 556 [10.1146/annurev-fluid-010816-060042](https://doi.org/10.1146/annurev-fluid-010816-060042) (_eprint: [https://doi.org/10.1146/annurev-fluid-](https://doi.org/10.1146/annurev-fluid-010816-060042)
 557 [010816-060042](https://doi.org/10.1146/annurev-fluid-010816-060042)) doi: 10.1146/annurev-fluid-010816-060042
- 558 Rubin, A. M., & Ampuero, J.-P. (2005). Earthquake nucleation on (aging) rate and state faults.
 559 *Journal of Geophysical Research: Solid Earth*, 110(B11). Retrieved 2023-01-12, from
 560 <https://onlinelibrary.wiley.com/doi/abs/10.1029/2005JB003686> (_eprint:
 561 <https://onlinelibrary.wiley.com/doi/pdf/10.1029/2005JB003686>) doi: 10.1029/2005JB003686
- 562 Ruina, A. (1983). Slip instability and state variable friction laws. *Journal of Geophysical Re-*
 563 *search: Solid Earth*, 88(B12), 10359–10370. Retrieved 2022-12-07, from [https://](https://onlinelibrary.wiley.com/doi/abs/10.1029/JB088iB12p10359)
 564 onlinelibrary.wiley.com/doi/abs/10.1029/JB088iB12p10359 (_eprint:
 565 <https://onlinelibrary.wiley.com/doi/pdf/10.1029/JB088iB12p10359>) doi: 10.1029/
 566 JB088iB12p10359
- 567 Sagy, A., Brodsky, E. E., & Axen, G. J. (2007, March). Evolution of fault-surface roughness with slip. *Ge-*
 568 *ology*, 35(3), 283–286. Retrieved 2024-02-04, from [https://doi.org/10.1130/G23235A](https://doi.org/10.1130/G23235A.1)
 569 .1 doi: 10.1130/G23235A.1
- 570 Scholz, C. H. (1989). *Mechanics of faulting*. (Publication Title: Annual review of earth and planetary sci-
 571 ences. Vol. 17 ISSN: 0084-6597) doi: 10.1146/annurev.ea.17.050189.001521
- 572 Shaw, B. E., & Rice, J. R. (2000). Existence of continuum complexity in the elastodynamics of re-
 573 peated fault ruptures. *Journal of Geophysical Research: Solid Earth*, 105(B10), 23791–23810.
 574 Retrieved 2023-12-27, from [https://onlinelibrary.wiley.com/doi/abs/10.1029/](https://onlinelibrary.wiley.com/doi/abs/10.1029/2000JB900203)
 575 [2000JB900203](https://onlinelibrary.wiley.com/doi/pdf/10.1029/2000JB900203) (_eprint: <https://onlinelibrary.wiley.com/doi/pdf/10.1029/2000JB900203>) doi:
 576 10.1029/2000JB900203
- 577 Taira, K., Brunton, S. L., Dawson, S. T. M., Rowley, C. W., Colonius, T., McKeon, B. J., ... Ukeiley, L. S.
 578 (2017, December). Modal Analysis of Fluid Flows: An Overview. *AIAA Journal*, 55(12), 4013–
 579 4041. Retrieved 2023-01-18, from <https://arc.aiaa.org/doi/10.2514/1.J056060>
 580 (Publisher: American Institute of Aeronautics and Astronautics) doi: 10.2514/1.J056060
- 581 Thomas, M. Y., Lapusta, N., Noda, H., & Avouac, J.-P. (2014). Quasi-dynamic versus fully dynamic
 582 simulations of earthquakes and aseismic slip with and without enhanced coseismic weakening.
 583 *Journal of Geophysical Research: Solid Earth*, 119(3), 1986–2004. Retrieved 2023-01-12, from
 584 <https://onlinelibrary.wiley.com/doi/abs/10.1002/2013JB010615> (_eprint:
 585 <https://onlinelibrary.wiley.com/doi/pdf/10.1002/2013JB010615>) doi: 10.1002/2013JB010615
- 586 Utsu, T., Ogata, Y., S, R., & Matsu'ura. (1995). The Centenary of the Omori Formula for a Decay Law of
 587 Aftershock Activity. *Journal of Physics of the Earth*, 43(1), 1–33. doi: 10.4294/jpe1952.43.1
- 588
- 589

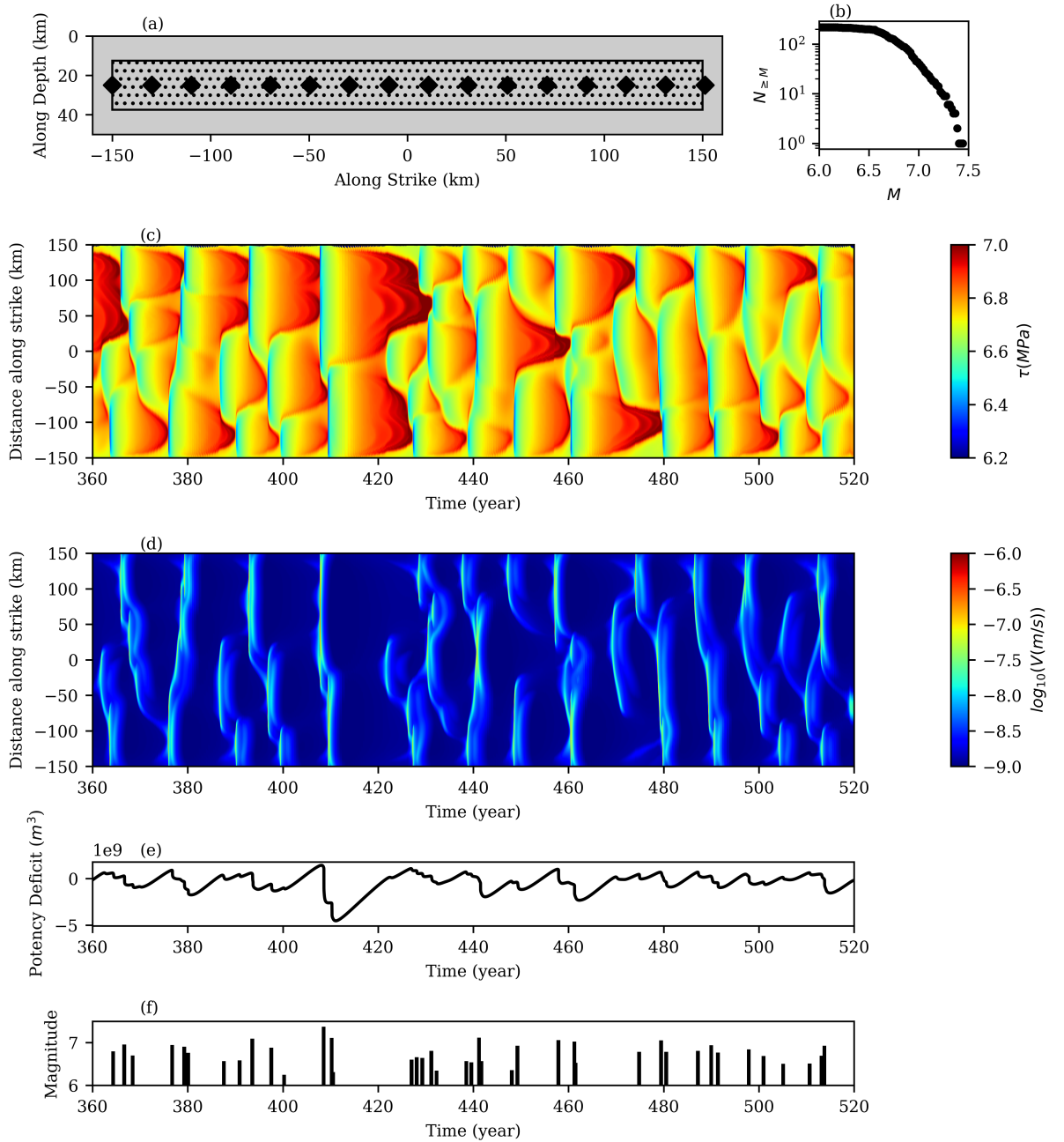


Figure 1. Geometry of the fault (a). The VW patch is the dotted area that is surrounded by the VS patch. The diamonds are the locations of slip rate measurements for the scenario in which we do not have full access to the slip rate on the entire fault. The number of events with a magnitude greater than M , (N_M) is plotted in (b) for 1000 years of simulation time. Maximum stress along the depth for the VW patch is plotted as a function of distance along strike and time (c). The maximum slip rate for the VW patch along the depth is plotted as a function of distance along strike and time (d). The time-series of the potency deficit and magnitudes are plotted in (e) and (f) respectively.

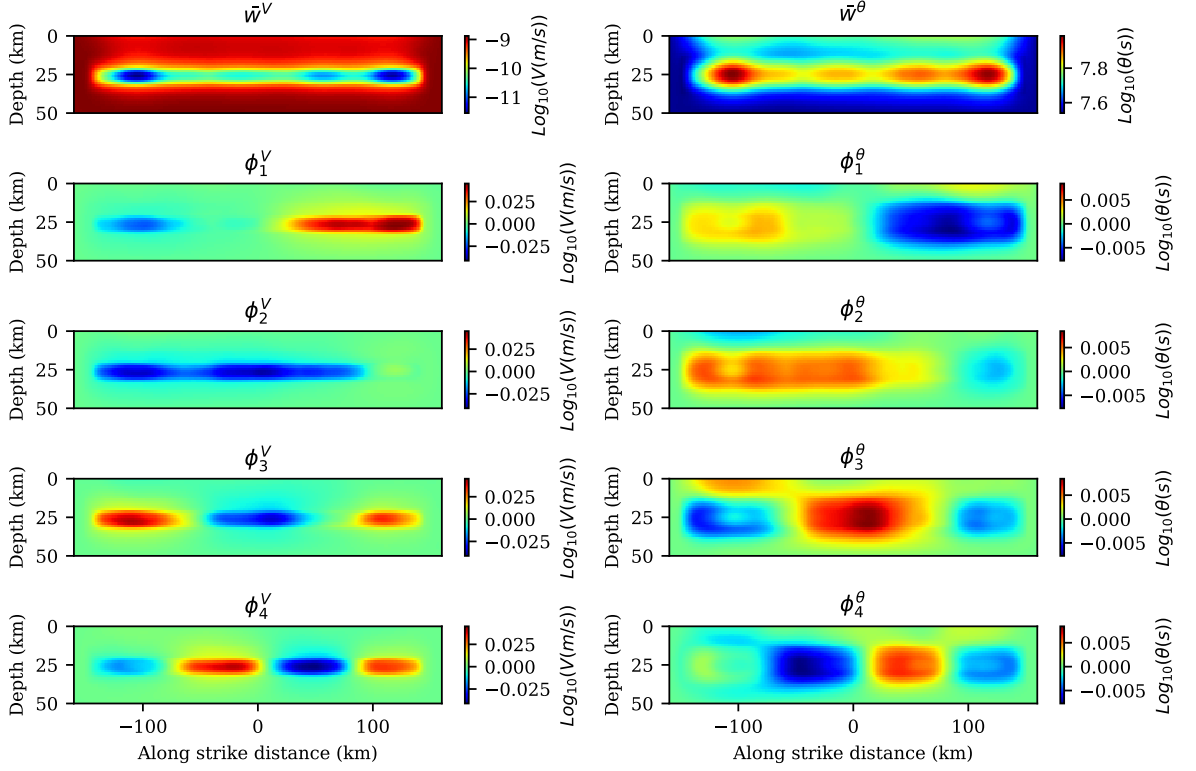


Figure 2. Average of the \log_{10} of slip rate (\bar{w}^V) and state variable (\bar{w}^θ) during the interevent periods, and first four eigenfunctions for \log_{10} of slip rate (ϕ_i^V for $1 \leq i \leq 4$) and state variable (ϕ_i^θ for $1 \leq i \leq 4$) that are ordered by the variance they capture in the datasets. The dataset contains interevent snapshots of \log_{10} of slip rate and state variable during the interevent periods from the year 200 to 1200.

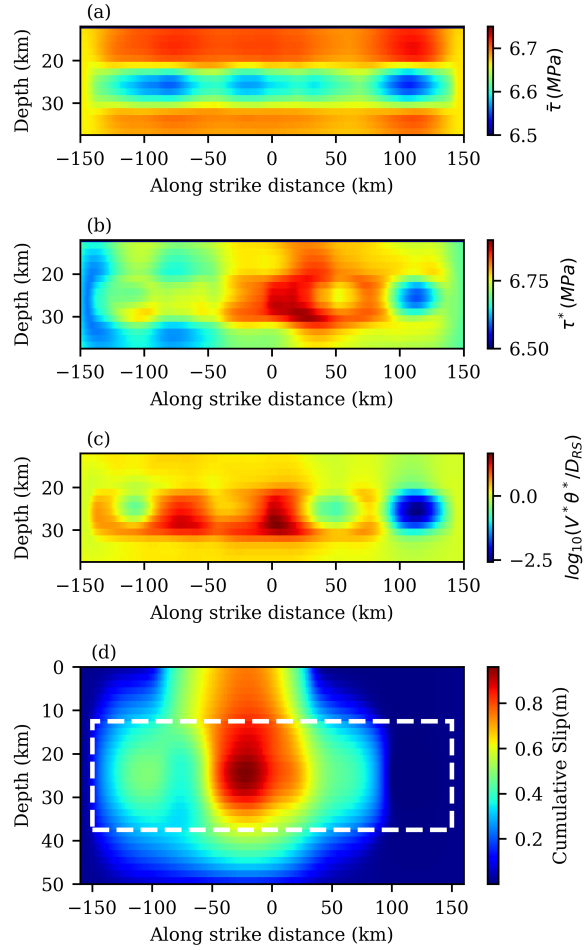


Figure 3. Average of the shear stress on the VW patch of the fault during the interevent period (a). One of the local optimal prestress distributions that leads to an event with a magnitude of 7.5 (b). The dimensionless quantity $\log_{10}(V\theta^*/D_{RS})$ for the optimal prestress is plotted in (c). The corresponding cumulative slip of the event that happens right after starting from optimal prestress (d). To increase the readability (a,b,c) are plotted only for the VW patch. The VW patch in (d) is denoted by the dashed white line.

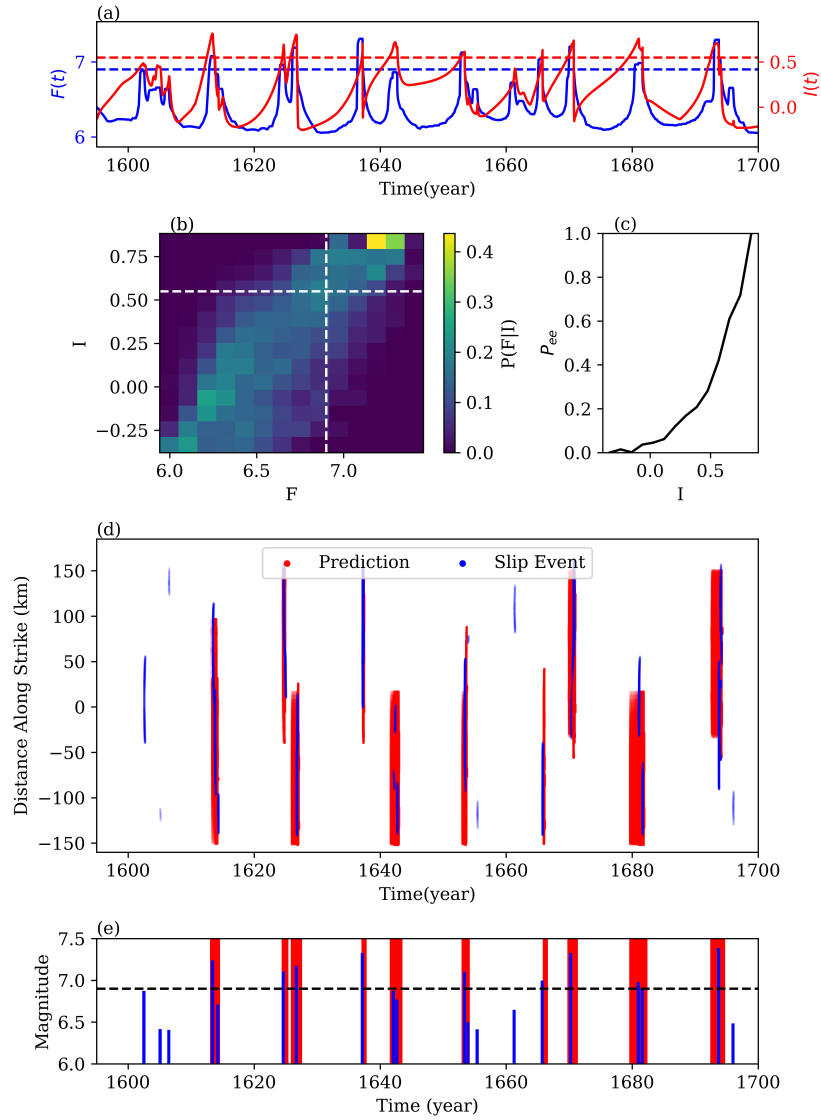


Figure 4. Spatiotemporal prediction of events. The time series of the functions F and I show that I rises when there is an upcoming large event (F is large), and it goes down when there is no upcoming large event. The blue and red dashed lines correspond to F_e and I_e (a). The empirical conditional probability $P(F|I)$. The vertical and horizontal dashed lines are F_e , and I_e respectively (b). The empirical probability of having an event with the value \tilde{M} greater than F_e in the next 0.5(year) as a function of the value of the indicator I (c). The spatiotemporal prediction of events is plotted by red where blue is the actual events in the dataset (d). Prediction of the magnitudes with the blue bars as the magnitude of events in the dataset. The horizontal axis for the blue bars denotes the time when an event starts. Red regions denote the times of high probability of large events (above magnitude 6.9 (dashed line)) based on our indicator (e). The statistical plots (b,c) are calculated based on 1000 years of data in the test set (data from the year 1200 to 2200)

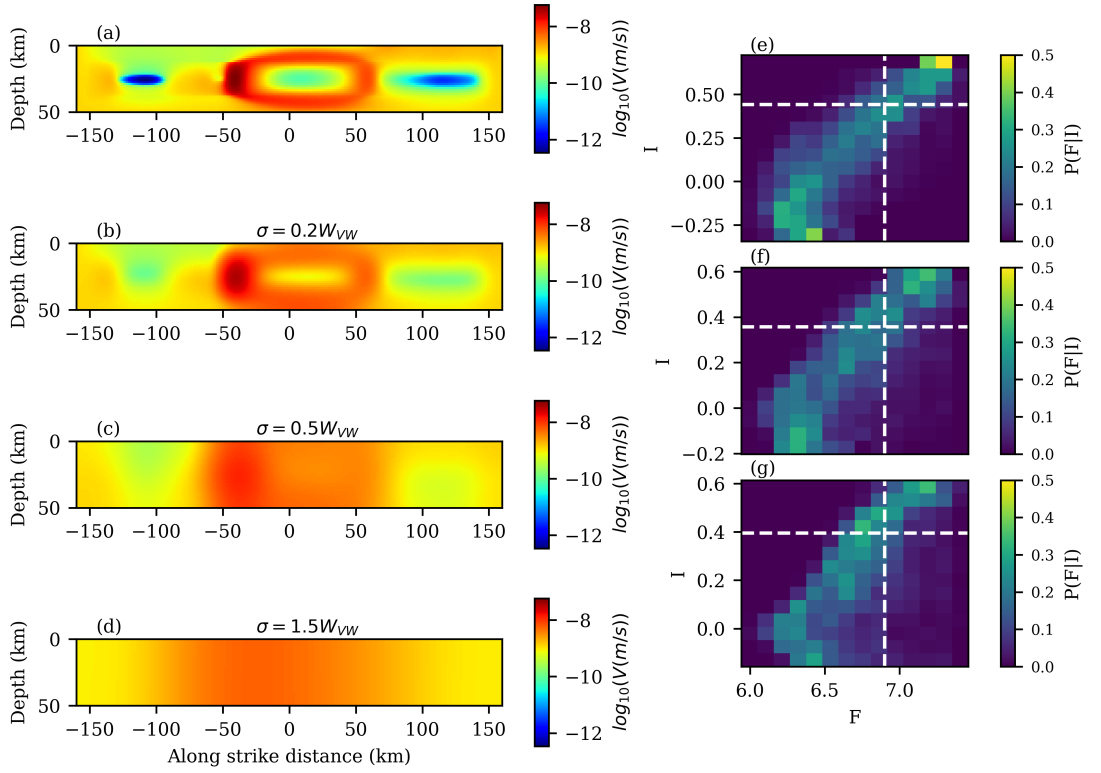


Figure 5. Impact of the low-pass filter noise on prediction. One snapshot of the slip rate is plotted in (a). To visualize the effect of noise, the low-pass filter applied to the snapshot in (a) is plotted in (b,c,d) with different standard deviations. The conditional probability of $P(F|I)$ when the slip rate is corrupted with a Gaussian low-pass filter with different noise standard deviations ($\sigma = 0.2W_{VW}$, $0.5W_{VW}$, $1.5W_{VW}$) are plotted in (e,f,g) respectively.

590 **Acknowledgments**

591 The authors HK and J-PA express their sincere gratitude to the National Science Foundation (NSF) for
592 their financial support of this research project, through the Industry-University Collaborative Research Center
593 Geomechanics and Mitigation of Geohazards (award #1822214). Author AMS is grateful to DoD for support
594 as a Vannevar Bush Faculty Fellow. Additionally, the authors are grateful for the valuable input and discussion
595 provided by Nadia Lapusta, Brendan Meade, Themis Sapsis, Adriano Gualandi, Alba Rodriguez, Camilla Cat-
596 tania, Elif Oral, Mateo Acosta, Kelian Dascher-Cousineau, Zachary R Ross, Jan Dirk Jansen, Kyungjae Im. The
597 authors also extend their appreciation to Eric Dunham and the other anonymous reviewer for their constructive
598 feedback and insightful comments.

Supporting Information for
Spatiotemporal forecast of extreme events in a dynamical model of earthquake sequences

Supp A Model

We use a model of a 2D thrust fault in a 3D medium governed by RS friction with aging law for the evolution of state variable (θ):

$$\frac{\tau}{\bar{\sigma}_n} = \mu^* + a \ln\left(\frac{V}{V^*}\right) + b \ln\left(\frac{\theta V^*}{D_{RS}}\right), \quad (\text{A1})$$

$$\frac{d\theta}{dt} = 1 - \frac{\theta V}{D_{RS}}. \quad (\text{A2})$$

Here $V(x, y, t) : \Gamma \times \mathbb{R}^+ \rightarrow \mathbb{R}^+$ is slip rate on the fault, $\theta(x, y, t) : \Gamma \times \mathbb{R}^+ \rightarrow \mathbb{R}^+$ is the state variable, $\tau(x, y, t) : \Gamma \times \mathbb{R}^+ \rightarrow \mathbb{R}^+$ is the frictional strength, $\bar{\sigma}_n$ is the effective normal stress, and a, b, D_{RS} are frictional properties of the surface (Γ) and are positive. μ^* and V^* are reference friction and slip rate respectively. The sign of $a - b$ determines the frictional regime of the fault. For $a - b > 0$, the fault is Velocity Strengthening (VS); a jump in the velocity would increase the fault strength. Regions with $a - b > 0$ suppress the rupture nucleation and acceleration. For $a - b < 0$ fault is Velocity Weakening (VW); a jump in the slip rate (V), decreases the strength, and the fault is capable of nucleating earthquakes and accelerating the ruptures. $a - b$ varies spatially and is plotted in Fig 1.

The stress rate on the fault can also be written as:

$$\dot{\tau} = \mathcal{L}(V - V_{pl}) - \frac{G}{2c_s} \dot{V} \quad (\text{A3})$$

where \mathcal{L} is a pseudo-differential operator, and contains most of the elastodynamic response (Geubelle & Rice, 1995). Function $V_{pl}(x, y)$ is the plate slip rate which is assumed to be constant in time in this work. We use quasi-dynamic approximation for \mathcal{L} , ignoring the wave-mediated effects on the fault surface (Geubelle & Rice, 1995). G and c_s are shear modulus and shear wave speed respectively. By taking the time derivative of Eq (A1), and eliminating $\dot{\tau}$ from the equations we have a dynamical system of the form of Eq (1) for $u = [V, \theta]^T$. We simulate the dynamical system from a non-symmetric initial condition (u_0) for 2200(*yr*) and remove the first 200(*yr*) to not include the transient behavior. The dynamical system based on this formalism can produce realistic cycles of earthquakes and SSEs. To justify the assumption of ignoring wave propagation effects along the fault, we use a parameter regime that produces SSEs in which V is small enough that the wave effects across the faults are negligible. We use model parameters and geometry used in (Dal Zilio et al., 2020) to simulate SSEs similar to those in Cascadia, except that for simplicity we did not include the effect of pore-pressure dilatancy. We use the QDYN software, which is an open-source code to simulate earthquake cycles (Luo et al., 2017). The frictional and physical properties of our problem are summarized in Table A1 and Fig 1. The maximum slip rate on the fault is plotted in Fig Supp1 with the dashed line as the threshold that we use for defining an event.

Table A1. Physical Properties

VW region	a	0.004
	b	0.014
VS region	a	0.019
	b	0.014
Characteristic slip weakening distance	D_{RS}	$0.045(m)$
Reference steady state slip rate	V^*	$10^{-6} \frac{m}{s}$
Reference steady-state friction coefficient	f^*	0.6
Effective normal stress	$\bar{\sigma}_n$	$10(MPa)$
Shear modulus	G	$30(GPa)$
Plate loading Velocity	V_{pl}	$40(mm/year)$

Supp B Proper Orthogonal Decomposition (POD): method and result

In this section, we review how to reduce the dimension of the dataset consisting of slip rate and state variable using the POD method. We use this method to find critical prestress in a low-dimensional space instead of the high-dimensional function space. Another reason to use this method is because Eq (7) is an optimization problem constrained on the chaotic attractor of the system with the event period excluded. To solve the constraint optimization problem (Eq (7)), one method (Farazmand & Sapsis, 2017) is to exclude the extreme events from the chaotic attractor and approximate the remaining using the POD technique. Here, we exclude the event period from the dataset to only approximate the interevent period. The method of approximating the chaotic attractor using POD modes is used in different fields. As an example, the work in (Blonigan et al., 2019) used 50 POD modes to approximate the chaotic attractor of a turbulent channel flow. One behavioral difference between our model of the earthquake cycle and the turbulent channel flow example is that the time stepping in our problem is adaptive due to the system's multi-scale behavior; there are more sample data when the dynamical system is stiff. However, since we are removing the event period from the data, we only include the slow part of the system in our dataset.

In the following paragraphs, we describe the POD analysis on our dataset of simulations. The data set comprises snapshots within the time span from the year 200 to 1200 excluding the event set ($E(V_{\text{thresh}})$). We use the time snapshots of discretized states of the system (θ and V) which belong to a high but finite-dimensional space. After discretization, $V : \mathbb{R}^{N_x \times N_y} \times \mathbb{R}^+ \rightarrow \mathbb{R}^+$ and $\theta : \mathbb{R}^{N_x \times N_y} \times \mathbb{R}^+ \rightarrow \mathbb{R}^+$. $N_x = 256$ and $N_y = 32$ are the numbers of grid points along the strike and depth respectively.

Since the evolution of the system is better realized in \log_{10} space, we apply the POD on the \log_{10} of the dataset. We define vectors $w_1(t_k)$ and $w_2(t_k)$ both in $\mathbb{R}^{N_x N_z}$ for time t_k as the vectorized form of the logarithm of V

and θ at time t_k .

$$w_1(t_k) = \log_{10} \left(\begin{array}{c} V_{1,1} \\ V_{1,2} \\ \vdots \\ V_{1,N_x} \\ V_{2,1} \\ V_{2,2} \\ \vdots \\ V_{2,N_x} \\ \vdots \\ V_{N_z,1} \\ V_{N_z,2} \\ \vdots \\ V_{N_z,N_x} \end{array} \right)_{t=t_k} \quad (\text{B1})$$

$$w_2(t_k) = \log_{10} \left(\begin{array}{c} \theta_{1,1} \\ \theta_{1,2} \\ \vdots \\ \theta_{1,N_x} \\ \theta_{2,1} \\ \theta_{2,2} \\ \vdots \\ \theta_{2,N_x} \\ \vdots \\ \theta_{N_z,1} \\ \theta_{N_z,2} \\ \vdots \\ \theta_{N_z,N_x} \end{array} \right)_{t=t_k} \quad (\text{B2})$$

where for example, by $[V_{i,j}]_{t_k}$, we mean slip rate at i^{th} element along strike and j^{th} element along the depth at k^{th} snapshots in the dataset. Then, we stack pairs of w_1 and w_2 to make a vector w :

$$w(t_k) = \begin{bmatrix} w_1(t_k) \\ w_2(t_k) \end{bmatrix} \in \mathbb{R}^{2N_x N_z}. \quad (\text{B3})$$

We define $\bar{w} = [\bar{w}^V, \bar{w}^\theta]^\top$ as the time average of $w(t_i)$ for all i in the dataset.

$$\bar{w} = \frac{1}{N_d} \sum_{i=1}^{N_d} w(t_i) \quad (\text{B4})$$

where N_d is the total number of snapshots in the dataset. \bar{w}^V and \bar{w}^θ are plotted in Fig 2. We define $p(t_k) = w(t_k) - \bar{w}$ and then we define a matrix $P \in \mathbb{R}^{2N_x N_z \times N_d}$ with the following entries:

$$P = [p(t_1) \ p(t_2) \ \cdots \ p(t_{N_d})] \in \mathbb{R}^{2N_x N_z \times N_d}. \quad (\text{B5})$$

Then, we define the covariance matrix R as the following:

$$R = \frac{1}{(N_d - 1)} P P^T \in \mathbb{R}^{2N_x N_z \times 2N_x N_z} \quad (\text{B6})$$

Now, we can find the eigenvectors of matrix R :

$$R\phi_j = \lambda_j\phi_j \quad \lambda_1 \geq \lambda_2 \geq \dots \geq \lambda_{2N_xN_y} \geq 0. \quad (\text{B7})$$

Eigenvalues show how well each eigenvector captures the original data in L^2 sense. Eigen-vectors of matrix R can be found using Singular Value Decomposition (SVD) of matrix P :

$$P = \Phi\Sigma\Psi^T \quad (\text{B8})$$

where in general $\Phi \in \mathbb{R}^{2N_xN_y \times 2N_xN_y}$ and $\Psi \in \mathbb{R}^{N_d \times N_d}$ are orthogonal ($\Phi\Phi^T = I_{2N_xN_y \times 2N_xN_y}$ and $\Psi\Psi^T = I_{N_d \times N_d}$) and determine, through columns, the left and right singular vectors of P ; and diagonal matrix $\Sigma \in \mathbb{R}^{2N_xN_y \times N_d}$ has singular values on its diagonal (Taira et al., 2017). We can write:

$$R = \frac{1}{(N_d - 1)} PP^T = \frac{1}{(N_d - 1)} \Phi\Sigma\Psi^T\Psi\Sigma^T\Phi^T$$

$$R\Phi = \frac{1}{(N_d - 1)} \Phi\Sigma\Sigma^T \quad (\text{B9})$$

because of the special form of Σ that will be discussed shortly, the columns of Φ (denoted here by ϕ_i and are plotted in Fig 2 for $i \leq 4$) are eigenvectors of matrix R that are ordered by the variance they capture in data. Note that $\phi_i \in \mathbb{R}^{2N_xN_y}$ and we can separate it into eigenvectors of the slip rate (ϕ_i^V) and the state variable ϕ_i^θ :

$$\phi_i = \begin{bmatrix} \phi_i^V \\ \phi_i^\theta \end{bmatrix} \quad (\text{B10})$$

Assuming the number of time snapshots is much smaller than the dimension of the problem $N_d \ll 2N_xN_y$, Σ has the following form:

$$\Sigma = \begin{bmatrix} \sigma_1 & 0 & 0 & 0 \\ 0 & \sigma_2 & 0 & 0 \\ \vdots & \vdots & \ddots & \vdots \\ 0 & 0 & 0 & \sigma_{N_d} \\ 0 & 0 & 0 & 0 \\ \vdots & \vdots & \vdots & \vdots \\ 0 & 0 & 0 & 0 \end{bmatrix}_{2N_xN_y \times N_d} \quad (\text{B11})$$

Then, using Eqs (B7), (B9), and (B11), $\frac{1}{(N_d-1)}\sigma_j^2 = \lambda_j$. λ_j corresponds to the variance of the data along ϕ_j . If λ_j goes to zero very fast, it suggests that we can explain the dataset in a low-dimensional subspace consisting of a finite number of eigenfunctions. The ratio $\sum_{j=1}^r \lambda_j / \sum_{j=1}^{N_d} \lambda_j$ shows the proportion of the variance of the data that are captured in the first r eigenfunctions. Based on Fig Supp2, the first 13 modes of the data capture almost 85% of the data.

Using this explanation, we can approximate the interevent period ($\mathcal{A} \setminus E(V_{\text{thresh}})$) by:

$$\log_{10}(\mathcal{A} \setminus E(V_{\text{thresh}})) \approx \left\{ w = \bar{w} + \sum_{i=1}^{N_m} a_i \phi_i \left| \sum_{i=1}^{N_m} \frac{a_i^2}{\lambda_i} \leq r_0^2 \right. \right\}. \quad (\text{B12})$$

where N_m is the number of modes (eigenfunctions) that are considered in the truncation. One can play with r_0 to enlarge the set. For very large r_0 the approximation is not valid anymore. The value of r_0 determines how much we let perturbation around the average of the dataset \bar{w} . As an example, taking $N_m = 1$ and $r_0 =$

1 would let perturbation around \bar{w} along ϕ_1 with an amplitude equal to the standard deviation of the dataset along that eigenvector ($\sqrt{\lambda_1}$).

Using the orthonormality of ϕ_i 's, we can find the projection of any $w(t)$ onto ϕ_i using the following inner product:

$$a_i(t) = \langle w(t) - \bar{w}, \phi_i \rangle \quad (\text{B13})$$

where $a_i(t)$ is the projection of $w(t) - \bar{w}$ onto eigenvector ϕ_i and \langle, \rangle denotes the inner product. We can find $a_i(t_k)$ for all of the time snapshots in the dataset and plot the distribution of $a_i/\sqrt{\lambda_i}$ (Fig Supp3). We see that the distribution is close to the standard normal distribution. Looking at this figure gives us intuition about choosing a value for r_0 . For example, selecting r_0 to be large (> 4), would lead to exploring low-probability regions. The dashed lines in the figure, correspond to $a_i/\sqrt{\lambda_i} = 1, 2, 3$.

Using the approximation in Eq (B12), we reduce the dimensionality of the system from $\mathbb{R}^{2N_x N_z}$ to \mathbb{R}^{N_m} and approximate a complicated set ($\mathcal{A} \setminus E(V_{\text{thresh}})$) by a hyperellipse which is a straightforward constraint for our optimization problem. With the mentioned approximation, and denoting $w^* = \bar{w} + \sum_{i=1}^{N_m} a_i^* \phi_i$, we write an optimization problem in the low dimensional \mathbb{R}^{N_m} space which is an equivalent approximate of Eq (7):

$$A^* = \{ \mathbf{a}^* \mid \sum_{i=1}^{N_m} \frac{a_i^{*2}}{\lambda_i} \leq r_0^2, w^* \text{ is a local maximizer of } F(10^{w^*}; \Delta t, T), F(10^{w^*}; \Delta t, T) > F_e^* \} \quad (\text{B14})$$

where $\mathbf{a}^* \in \mathbb{R}^{N_m}$ whose i^{th} element is a_i^* . Eq (B14) ensures that the optimal solutions are not too far from the mean states (\bar{w}).

To show the applicability of the POD model reduction outside the application of this paper, we also applied the method to a dataset including all snapshots within the period of 200 years to 1200 years (without removing the event period). The result of this model reduction is available in Supplemental Video 2. This video shows that we can capture all phases of earthquake cycles using a few POD modes.

Supp C Optimization

Here we revisit optimal sampling in the framework of Bayesian optimization as discussed in (Brochu et al., 2010) and is improved in (Blanchard & Sapsis, 2021) for finding the precursors of extreme events. The optimization algorithm works by exploring the input space ($\mathbf{a} = [a_1, \dots, a_{N_m}] \in \mathbb{R}^{N_m}$) using a Gaussian surrogate model. Suppose that we want to solve the constrained optimization problem of Eq (7) with the approximation in Eq (8). Without loss of generality, we study the minimization of the minus sign of the cost function ($G = -F$) instead of maximizing it. The cost function can be evaluated using a forward simulation of a given initial condition. Here we assume that the observation is contaminated by a small Gaussian noise with variance $\sigma_\epsilon^2 = 10^{-4}$.

$$z = G(a; T, \Delta t) + \epsilon \quad \epsilon \sim \mathcal{N}(0, \sigma_\epsilon^2) \quad (\text{C1})$$

where ϵ is the observational noise, and T and Δt are hyperparameters of the cost function G that are determined before the optimization process. The iterative approach starts from some randomly sampled N_{init} points $\{\mathbf{a}_k \in \mathbb{R}^{N_m}\}_{k=1}^{N_{init}}$ that each of them corresponds to a point in the set defined in (8). Using the forward model of Eq (C1) we find the input-output pair $\mathcal{D}_0 = \{\mathbf{a}_k, z_k\}_{k=1}^{N_{init}}$. $\mathbf{a}_k \in \mathbb{R}^{N_m}$ is the vector of POD coefficients with N_m as the number of POD modes we have decided to consider, and z_k comes from Eq (C1). Using a Gaussian surrogate model, the expected value and variance of the process, condition on the input/output at each step i (\mathcal{D}_i) is given by the following equation:

$$\begin{aligned} \mu(\mathbf{a}) &= m_0 + k(\mathbf{a}, \mathbf{A}_i) \mathbf{K}_i^{-1} (\mathbf{z}_i - m_0) \\ \sigma^2(\mathbf{a}) &= k(\mathbf{a}, \mathbf{a}) - k(\mathbf{a}, \mathbf{A}_i) \mathbf{K}_i^{-1} k(\mathbf{A}_i, \mathbf{a}) \end{aligned} \quad (\text{C2})$$

where $\mathbf{K}_i = k(\mathbf{A}_i, \mathbf{A}_i) + \sigma_\epsilon^2 \mathbf{I}$, $\mathbf{A}_i = \{\mathbf{a}_k\}_{k=1}^{N_{init}+i}$, and $\mathbf{z}_i = \{z_k\}_{k=1}^{N_{init}+i}$. We consider the Radial Basis Function (RBF) with Automatic Relevance Determination (ARD):

$$k(\mathbf{a}, \mathbf{a}') = \sigma_f^2 \exp(-(\mathbf{a} - \mathbf{a}')^T \Theta^{-1} (\mathbf{a} - \mathbf{a}') / 2) \quad (\text{C3})$$

where Θ is a diagonal matrix containing the length scale for each dimension. At each iteration, we construct a surrogate model (Eq (C2)). Then, the next point in the input space is found by minimizing an acquisition function ($g : \mathbb{R}^{N_m} \rightarrow \mathbb{R}$). We use the **Lower Confidence Bound** (LCB) acquisition function which is defined as the following:

$$g_{LCB}(\mathbf{a}) = \mu(\mathbf{a}) - \kappa \sigma(\mathbf{a}) \quad (\text{C4})$$

where κ is a positive number that balances exploration and exploitation. For small κ , we do not consider uncertainties of the surrogate model and trust the mean of the conditional Gaussian process. For large κ , minimizing Eq (C4) is equivalent to finding a point that has the largest uncertainty. We use $\kappa = 1$ in this study. The algorithm is extracted from Ref (Blanchard & Sapsis, 2021) and is summarized in Algorithm 1. We start the algorithm by randomly sampling 10 initial points inside the hyper-ellipse (Eq (8)) and then augmenting the input-output pairs by minimizing the acquisition function until the size of the input-output points reaches 200. To show the effectiveness of the algorithm in finding optimal solutions, we define the function c as the following:

$$c(i) = - \min_{1 \leq j \leq i} \min_{\mathbf{a}} \mu(\mathbf{a} | \mathcal{D}_j) \quad (\text{C5})$$

To find $c(i)$, we need to find the minimum of the Gaussian process in each iteration i and report the minimum over all $1 \leq j \leq i$. The algorithm does not guarantee finding all of the local maxima. As a result, the algorithm is repeated for 30 trials with different randomly chosen initial points. The behaviour of $c(i)$ for different values of r_0 is plotted in Fig Supp4 (a). The solid line is the median of $c(i)$ for different trials as a function of iteration and the shaded band shows half of the median absolute deviation. One of the optimal solutions is plotted in Fig Supp4 (b,c). During the optimization process, we augment the set W^* if the condition in Eq (9) is satisfied.

Algorithm 1 Bayesian Optimization

- 1: **Input:** Number of initial points n_{init} and number of iterations n_{iter}
- 2: **Initialize:** Surrogate model on initial dataset $\mathcal{D}_0 = \{\mathbf{a}^{(k)}, z^{(k)}\}_{k=1}^{n_{init}}$
- 3: **for** $n=0$ to n_{iter} **do**
- 4: Select best next point \mathbf{a}_{n+1} by minimizing acquisition function constrained inside the hyperellipse (Eq (8)):

$$\mathbf{a}^{(n+1)} = \arg \min_{\sum_{i=1}^{N_m} \frac{a_i^2}{\lambda_i} \leq r_0^2} g_{LCB}(\mathbf{a}; \bar{G}, \mathcal{D}_n)$$

- 5: Evaluate objective function G at $\mathbf{a}^{(n+1)}$ and record $z^{(n+1)}$
 - 6: If $z^{(n+1)} < -F_e^*$ augment the set W^* (Eq (9))
 - 7: Augment dataset $\mathcal{D}_{n+1} = \mathcal{D}_n \cup \{\mathbf{a}_{n+1}, z_{n+1}\}$
 - 8: Update surrogate model
 - 9: **end for**
-

Supp D Forecast with Partial Observation of Slip Rate

So far, we have assumed that we have full access to the slip rate on the fault. Here, we relax this assumption and use slip rate measurements only at a few points on the fault (diamonds in Fig 1 (a)). We denote $\hat{V} : \mathbb{Z}^{N_p} \times \mathbb{R}^+ \rightarrow \mathbb{R}^+$ as the time series of partial slip rate observation, where N_p is the number of points of slip rate measurements and we take it to be 16 in this case study. We assume that these points are at the center of the fault along the depth and have equal distances along the strike. We redefine the indicator $I(t)$ for this special case as follows:

$$I(t) = \max_i \frac{\left\langle \log \hat{V}(t) - \hat{w}^V, \log \hat{V}_i^* - \hat{w}^V \right\rangle_{\mathbb{R}^{N_p}}}{\| \log \hat{V}(t) - \hat{w}^V \|_2 \| \log \hat{V}_i^* - \hat{w}^V \|_2} \quad (\text{D1})$$

where \hat{V}_i^* is the slip rate at the measurement points (diamonds in Fig 1 (a)) of the i^{th} optimal solution in the set W^* . \hat{w}^V is the average slip rate at the measurement points during the interevent period. $\langle \cdot, \cdot \rangle_{\mathbb{R}^{N_p}}$ is the inner product in \mathbb{R}^{N_p} . Fig Supp5 shows the forecast performance in the limited slip rate measurement scenario. The general consistent increase in $I(\cdot)$ when the function $F(\cdot)$ rises is visible in Fig Supp5 (a). Fig Supp5 (b) and (c) show statistically the performance of the predictor. While most of the probability mass of $P(F|I)$ belongs to true positive and true negative we should appreciate that there is more probability mass in the false positive quadrant compared to the scenario in which we have full access to the slip rate. This can be observed better in Fig Supp5 (c), (d), and (e). Although as I increases, P_{ee} increases consistently, P_{ee} is almost 0.9 when I is the maximum which suggests that there is a 10% chance of a false positive signal when I takes its maximum value. This false positive can also be observed in Fig Supp5 (d) and (e) around the year 1610. While it is important to appreciate the limitations, the overall performance is satisfying. To reduce this limitation, one can use filtering methods to invert and approximate slip rates at a few more points on the fault to improve the performance.

Supplemental Figures

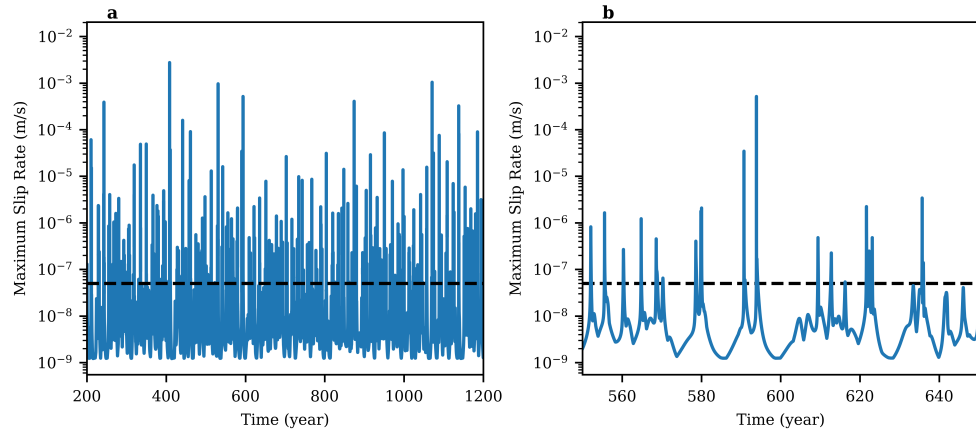


Figure Suppl. Time series of the maximum slip rate for a period of 1000 years (a) and 100 years (b) with threshold velocity denoted by a dashed line.

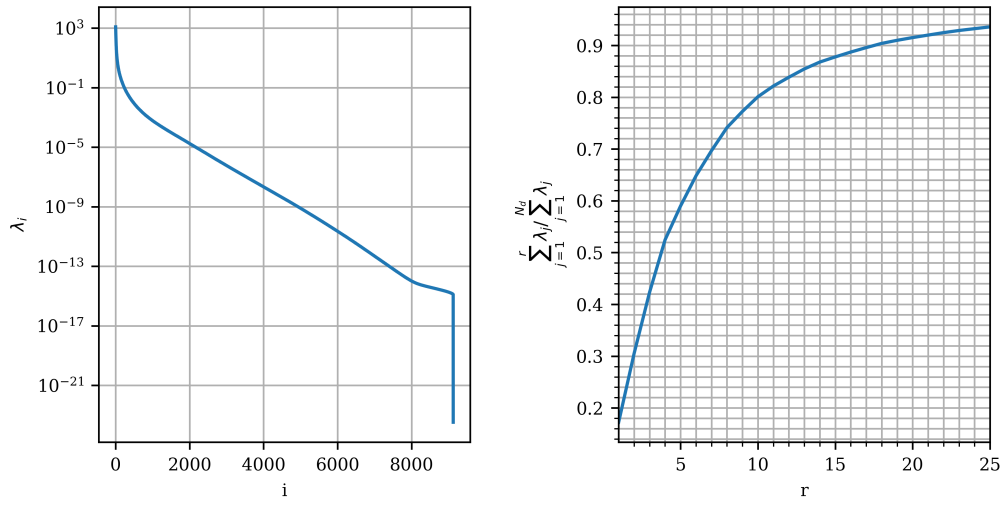


Figure Supp2. Convergence of the eigenvalues (left) and the ratio of a truncated sum of eigenvalues to the total sum of eigenvalues (right).

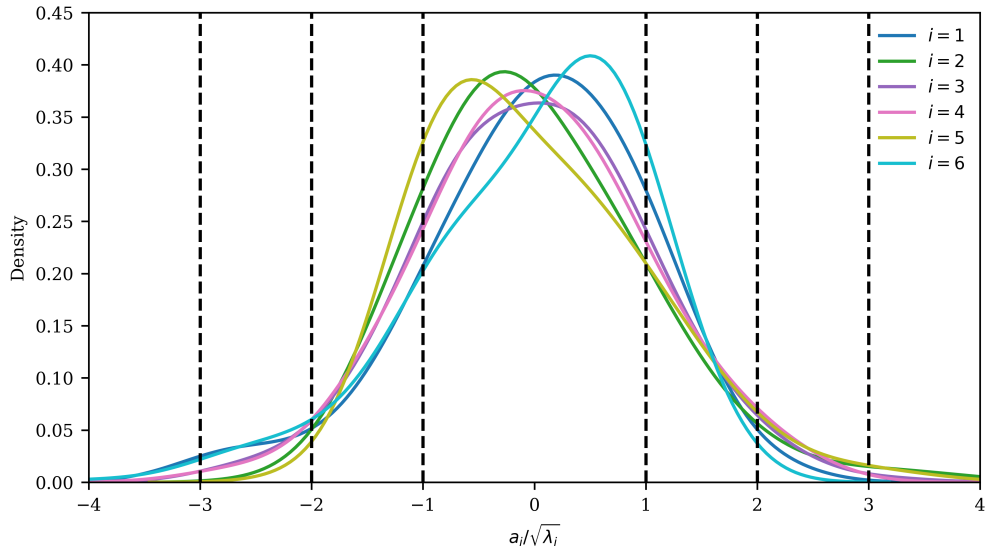


Figure Supp3. The distribution of $a_i(t)/\sqrt{\lambda_i}$ in the dataset of the interevent periods. The vertical lines correspond to $a_i/\sqrt{\lambda_i} = \pm 1, \pm 2, \pm 3$ and are plotted to give insight for selecting proper r_0 in Eq (8)

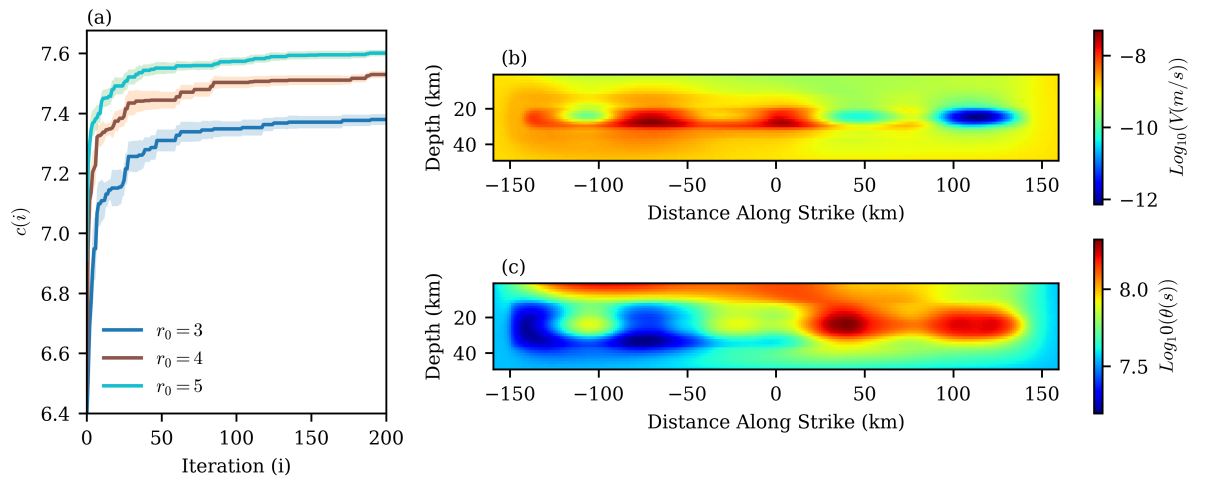


Figure Supp4. Convergence of the optimization for different values of r_0 (a). $\log_{10}(V)$ and $\log_{10} \theta$ of one of the optimal solutions with $r_0 = 3$ which leads to a magnitude 7.5. The optimal solution is highly heterogeneous and shows the effect of favorable stress heterogeneity in generating big events (b,c). The stress calculated from this optimal solution is plotted in 3

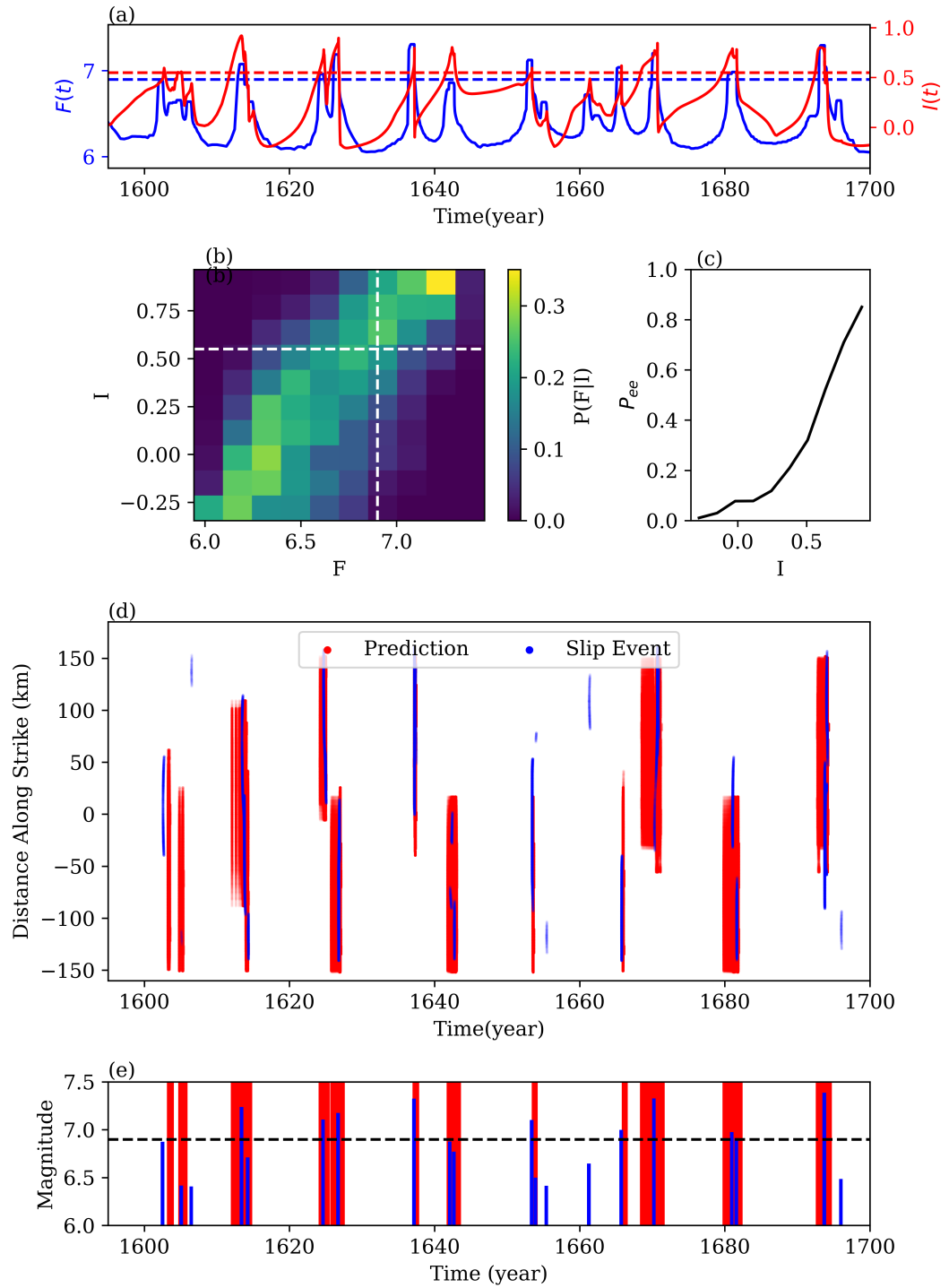


Figure Supp5. Spatio-temporal prediction of events same as in Fig 4 but using slip rate only at 16 points on the fault (denoted in Fig 1 (a) by diamonds)